Laminar flow in a channel bounded by porous/rough walls: Revisiting Beavers-Joseph-Saffman

Essam Nabil Ahmed *, Alessandro Bottaro

DICCA, Università di Genova, via Montallegro 1, Genova, 16145, Italy

ARTICLE INFO

ABSTRACT

The fully developed, steady, incompressible, laminar flow in a channel delimited by rough and/or permeable walls is considered. The influence of the micro-structured bounding surfaces on the channel flow behavior is mimicked by imposing high-order effective boundary conditions which stem from homogenization theory and do not contain empirical parameters. A closed-form solution of the Navier–Stokes equations is found for the flow in the channel, with conditions at each virtual boundary linking the slip velocities to shear stress and streamwise pressure gradient. The boundary condition for the longitudinal velocity coincides with a little-noticed extension of the so-called Beavers-Joseph condition, first derived by Saffman (1971); it applies to both permeable and rough surfaces, including the case of separated flow (Couette-Poiseuille motion with adverse pressure gradient). The analytical solution obtained for the velocity distribution in the channel is validated against full feature-resolving simulations of the flow for either highly ordered or random textures, highlighting the accuracy and the applicability range of the model. The Stokes-based model used to identify slip and interface permeability coefficients in the effective boundary conditions is found to be reliable and accurate up to $\epsilon Re_\tau \approx 10$, with ϵ ratio of microscopic to macroscopic length scales and Re_τ the shear-velocity Reynolds number. Above this threshold, the coefficients must account for advective effects: a new upscaling procedure, based on an *Oseen's approximation*, is thus proposed and validated, extending considerably beyond the Stokes regime.

1. Introduction

The low-Reynolds-number motion of an incompressible fluid in a plane channel bounded by a porous wall which borders the duct in $\hat{y} = 0$ has been a classical problem since the seminal experimental work by Beavers & Joseph [1]. They observed that the flow rate in the channel was larger in the presence of the porous layer than with a no-slip wall and hypothesized that the fluid could slip at some *Stokes–Darcy interface* with velocity

$$\hat{u}_{slip} = \frac{\sqrt{\hat{\mathcal{K}}}}{\alpha} \frac{\partial \hat{u}}{\partial \hat{y}}\bigg|_{\hat{y}\to 0^+} + \frac{\hat{\mathcal{K}}}{\mu} \mathcal{M}, \qquad (1)$$

with the second term on the r.h.s. of Eq. (1) corresponding to Darcy's velocity; $\hat{\mathcal{K}}$ is a scalar measure of the permeability of the porous medium in its bulk, μ is the dynamic viscosity, and $\mathcal{M} = |\partial \hat{p}/\partial \hat{x}|$ denotes the magnitude of the macroscopic, streamwise pressure gradient. The dimensionless constant α was later observed to depend on the properties and the geometry of the permeable material near the dividing surface, on the local direction of the flow, on the Reynolds number and on the possible presence of structural non-uniformities

at the surface of the porous medium, where the porosity is locally larger [2,3]. Such non-uniformities are hardly avoidable in practice since solid inclusions cannot pack as tightly near the porous/free-fluid interface as they do in the bulk of the porous medium [4].

Saffman [5] gave a theoretical justification of the empirical condition by Beavers & Joseph [1] by first applying ensemble averaging to the Stokes equation across the porous/free-fluid domain and then performing asymptotic matching at the two edges of the interface layer. A closer look at Saffman's development reveals that, upon retaining terms up to second order in the small parameter $\sqrt{\hat{\mathcal{K}}}$, the slip velocity is the same as in Eq. (1) except for Darcy's term, which was found to be corrected by an order one dimensionless factor B, to become $(B\hat{\mathcal{K}}/\mu)\mathcal{M}$. The literature is rich of studies that sought to revisit/extend/generalize the Beavers-Joseph-Saffman (BJS) condition and/or investigate its limitations and deficiencies, e.g. Refs. [6–11].

Some of the papers that followed the works by Beavers, Joseph and Saffman used upscaling theories to close the problem and identify the constant α (and, rarely, also B). Among the major contributors, extensively cited in the recent review by Bottaro [12], we count Mikelić

* Corresponding author.
   E-mail address: essameldin.abdo@edu.unige.it (E.N. Ahmed).

and colleagues (using asymptotic homogenization) and Whitaker and colleagues (using volume averaging). Recent papers are those by Lācis & Bagheri [13], Lācis et al. [14], Sudhakar et al. [15], and Naqvi & Bottaro [16], where homogenization theory was brought to second order in terms of a small parameter, ratio of microscopic to macroscopic length scales, for the BJS condition to read (for the channel flow case):

$$\hat{u}_{slip} = \hat{\lambda}\,\frac{\partial \hat{u}}{\partial \hat{y}}\bigg|_{\hat{y}\to 0^+} + \frac{\hat{\mathcal{K}}^{itf}}{\mu}\,\mathcal{M}; \tag{2}$$

the coefficients $\hat{\lambda}$, a *Navier slip length*, and $\hat{\mathcal{K}}^{itf}$, the *interface permeability*, are not simply proportional to $\sqrt{\hat{\mathcal{K}}}$ and $\hat{\mathcal{K}}$, and can be found by solving microscopic (*auxiliary*) problems in a representative unit cell, for any regular microscopic pattern. It should be highlighted that: (*i*) the BJS condition (2) is valid for both permeable and rough, impermeable layers (in the latter case $\hat{\mathcal{K}}$ vanishes, whilst $\hat{\lambda}$ and $\hat{\mathcal{K}}^{itf}$ do not); (*ii*) computed values of $\hat{\lambda}$ and $\hat{\mathcal{K}}^{itf}$ are available in the literature for many rough [14,15,17–19] and porous [14–16,20] wall microstructures; (*iii*) the theory is not limited to the simple case of plane channels; several examples with complex geometries are provided in the references given above. In the general case, Eq. (2) must be coupled to a zero-net mass flux condition for the wall-normal speed $\hat{v}$ at the virtual interface [14]. Such transpiration becomes crucial when the flow is turbulent [12,14], but is of no concern in the present fully developed flow setting, as shown later.

In view of the aforementioned contributions, the authors believe that a comprehensive investigation that addresses and systematically pursues answers to the following critical questions regarding the boundary condition (2) is still needed:

i. How versatile is it for different wall patterns/textures?
ii. How does it perform when the microscopic and macroscopic length scales are comparable?
iii. Is accuracy enhanced when we advance in the order of the asymptotic approximation?
iv. Is it accurate in the presence of near-wall backflow?
v. Is the condition still valid beyond the Stokes flow regime?
vi. Can it be further improved, in the presence of sizeable near-wall advective effects, such that its applicability range is extended?

The purpose of this article is to highlight the extent of the validity of the BJS condition (2) when rough and/or permeable layers, of either isotropic or transversely isotropic microstructure in the $(\hat{x} - \hat{z})$ plane, delimit the flow, including the case of positive pressure gradient with flow separation; we further aim to show the effectiveness of homogenization theory to evaluate the macroscopic coefficients, $\hat{\lambda}$ and $\hat{\mathcal{K}}^{itf}$, for a wide range of surface/substrate microstructures. The goals above are accomplished by finding the analytical solutions of the Navier–Stokes equation for the Poiseuille and the combined Couette-Poiseuille problems in the channel, subject to slip boundary conditions, and comparing them to numerical simulations of the flow in both the channel and the porous/rough layer, with full resolution of the small-scale flow features within the pores and/or the textured surface(s). Moreover, a procedure is outlined to treat the case in which near-wall advection becomes relevant, illustrating how slip and surface permeability coefficients vary.

The basic homogenization approach is presented in Section 2 and the macroscopic coefficients are evaluated for a collection of surface patterns. In Section 3, the analytical solutions are derived and validated. Finally, a novel version of the homogenization approach, accounting for advection via an Oseen-based approach, is described and its advantages over the Stokes-based model are thoroughly discussed. Concluding remarks are provided in Section 4.

2. The homogenization model

2.1. Upscaling procedure and effective boundary conditions

The incompressible, isothermal, steady, laminar flow in a channel of height $2H$ bounded from the bottom and the top sides (subscripts *b* and *t* respectively) by rough/permeable walls, i.e. at $\hat{y}_b = 0$ and $\hat{y}_t = 0$, is analyzed; cf. Fig. 1(*a*). The dimensional mass and momentum conservation equations governing the distribution of the velocity vector (whose components are denoted as $\hat{u}_1 = \hat{u}$, $\hat{u}_2 = \hat{v}$, $\hat{u}_3 = \hat{w}$) and the modified pressure $\hat{p}$ over space ($\hat{x}_{1,b(t)} = \hat{x}_{b(t)}$, $\hat{x}_{2,b(t)} = \hat{y}_{b(t)}$, $\hat{x}_{3,b(t)} = \hat{z}_{b(t)}$) are

$$\frac{\partial \hat{u}_i}{\partial \hat{x}_i} = 0, \quad \rho \hat{u}_j\frac{\partial \hat{u}_i}{\partial \hat{x}_j} = -\frac{\partial \hat{p}}{\partial \hat{x}_i} + \mu\frac{\partial^2 \hat{u}_i}{\partial \hat{x}_j^2}, \tag{3}$$

based on either of the two coordinate systems; ρ is the fluid density and μ is the dynamic viscosity. The channel flow is influenced by the presence of the micro-structured boundaries where a complex, generally three-dimensional interaction takes place as the fluid passes near/within the surface corrugations. The presence of well-separated length scales, i.e. the microscopic scales ℓ_b and ℓ_t characterizing the bottom and top surfaces/substrates, respectively, and the macroscopic length scale (chosen here as H, half the channel height), renders the problem amenable to upscaling via the multiscale homogenization approach; *effective* boundary conditions of the velocity can be derived at fictitious plane interfaces, next to the physical rough/porous boundaries, to mimic the effects of small surface inhomogeneities on the macroscopic channel flow.

The homogenization approach adopted here proceeds along the same lines of Naqvi & Bottaro [16] and Ahmed et al. [20]. The whole flow domain is first decomposed into macroscopic and microscopic sub-domains, and virtual matching interfaces (at $\hat{y}_b = \hat{y}_{\infty,b}$ and $\hat{y}_t = \hat{y}_{\infty,t}$; cf. Fig. 1(*b*)) are defined where continuity of velocity and traction vectors is applied. An asymptotic analysis is then conducted on the microscopic problems (bottom/top), which are accordingly reconstructed at different orders of the small parameters $\epsilon_{b(t)} = \ell_{b(t)}/H$. At each order, a generic solution of the problem considered is assumed, in which auxiliary, newly introduced, purely microscopic variables appear; systems of partial differential equations permit to numerically evaluate these variables (discussed in more detail in Section 2.2) and to define, via an averaging procedure, the upscaled coefficients which enter directly the effective boundary conditions at the matching interface(s). In particular, it is convenient to eventually set $\hat{y}_{\infty,b(t)}$ to 0 and, hence, to evaluate the macroscopic coefficients for matching interface(s) passing by the tips/crests/outer rims of the ribs (or the first row of inclusions); cf. Fig. 1. The homogenized boundary conditions, valid up to second-order in terms of $\epsilon_{b(t)}$, can be formally expressed in the following dimensional form:

$$\hat{u}|_0 \approx \underbrace{\hat{\lambda}_x\left(\frac{\partial \hat{u}}{\partial \hat{y}} + \frac{\partial \hat{v}}{\partial \hat{x}}\right)\bigg|_0}_{\text{First order}} + \underbrace{\frac{\hat{\mathcal{K}}_{xy}^{itf}}{\mu}\frac{\partial}{\partial \hat{x}}\left(-\hat{p} + 2\mu\frac{\partial \hat{v}}{\partial \hat{y}}\right)\bigg|_0}_{\text{Second order}}, \tag{4}$$

$$\hat{v}|_0 \approx \underbrace{\frac{\hat{\mathcal{K}}_{yy}}{\mu}\left(-\frac{\partial \hat{p}}{\partial \hat{y}} + 2\mu\frac{\partial^2 \hat{v}}{\partial \hat{y}^2}\right)\bigg|_0 - \hat{\mathcal{K}}_{xy}^{itf}\frac{\partial}{\partial \hat{x}}\left(\frac{\partial \hat{u}}{\partial \hat{y}} + \frac{\partial \hat{v}}{\partial \hat{x}}\right)\bigg|_0 - \hat{\mathcal{K}}_{zy}^{itf}\frac{\partial}{\partial \hat{z}}\left(\frac{\partial \hat{w}}{\partial \hat{y}} + \frac{\partial \hat{v}}{\partial \hat{z}}\right)\bigg|_0}_{\text{Second order}},$$
$$\tag{5}$$

$$\hat{w}|_0 \approx \underbrace{\hat{\lambda}_z\left(\frac{\partial \hat{w}}{\partial \hat{y}} + \frac{\partial \hat{v}}{\partial \hat{z}}\right)\bigg|_0}_{\text{First order}} + \underbrace{\frac{\hat{\mathcal{K}}_{zy}^{itf}}{\mu}\frac{\partial}{\partial \hat{z}}\left(-\hat{p} + 2\mu\frac{\partial \hat{v}}{\partial \hat{y}}\right)\bigg|_0}_{\text{Second order}}, \tag{6}$$

evaluated at the boundary of interest (either $\hat{y}_b = 0$ or $\hat{y}_t = 0$).

An in-depth look at these expressions reveals that the no-slip boundary conditions for the streamwise and the spanwise velocity components (respectively, $\hat{u}$ and $\hat{w}$) are corrected at first order by the classical Navier-slip conditions and at second order by the gradients of the normal stress, while a transpiration velocity, $\hat{v}$, at the fictitious wall in $\hat{y}_{b(t)} = 0$ appears only at second order. The dimensional groups of coefficients, i.e. the Navier-slip lengths in the streamwise and the spanwise
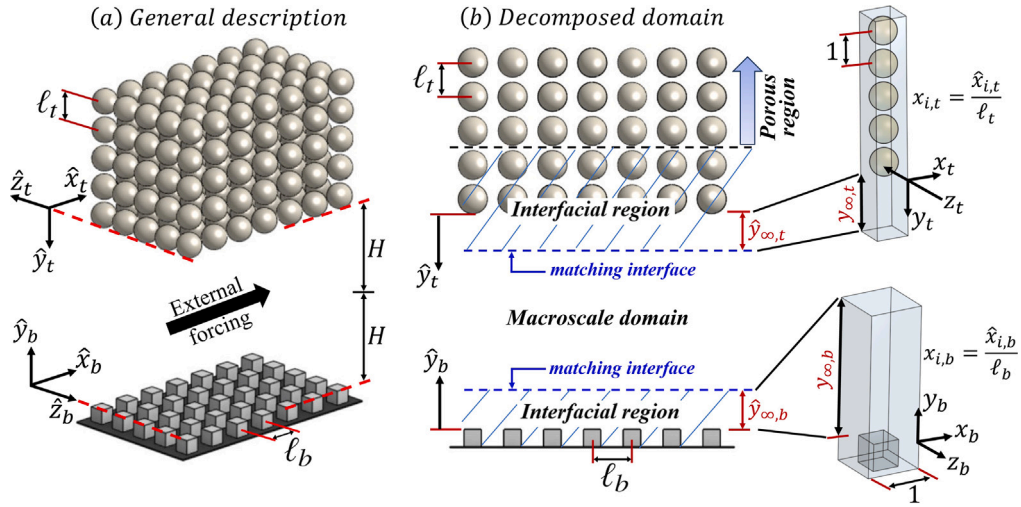
Fig. 1. Sketch of the hierarchical flow problem under analysis, with indication of the microscopic/macroscopic length scales. The domain decomposition is illustrated in panel (b), and doubly periodic elementary cells (periodicity here is in the x and z directions) of the top and bottom microscopic domains are shown in the right frame, with their dimensions described in the dimensionless coordinates $x_{i,b(t)}$.

directions ($\hat{\lambda}_{x,b(t)}$, $\hat{\lambda}_{z,b(t)}$), and the interface and intrinsic permeability coefficients ($\hat{\mathcal{K}}^{itf}_{xy,b(t)}$, $\hat{\mathcal{K}}^{itf}_{zy,b(t)}$, $\hat{\mathcal{K}}_{yy,b(t)}$) are homogeneous to, respectively, a length and a surface area, and correspond to the product of their dimensionless counterparts times, respectively, $l_{b(t)}$ and $l^2_{b(t)}$, that is

$$\hat{\lambda}_x = \lambda_x l, \quad \hat{\lambda}_z = \lambda_z l, \tag{7}$$

$$\hat{\mathcal{K}}^{itf}_{xy} = \mathcal{K}^{itf}_{xy} l^2, \quad \hat{\mathcal{K}}^{itf}_{zy} = \mathcal{K}^{itf}_{zy} l^2, \quad \hat{\mathcal{K}}_{yy} = \mathcal{K}_{yy} l^2. \tag{8}$$

The dimensionless macroscopic coefficients are dependent only on the micro-structural details of the corresponding surface/substrate, for instance the protrusion size-to-pitch ratio and the porosity[1] (θ) for, respectively, the rough surface and the permeable bed sketched in Fig. 1. In other words, these coefficients are intrinsic to the geometric characteristics of the boundary and do not depend on the Reynolds number; the effective boundary conditions up to second-order accuracy in terms of ϵ requires considering the reconstructed microscopic problems at $\mathcal{O}(\epsilon^0)$ and $\mathcal{O}(\epsilon^1)$ [20] where the inertial terms are not yet present. For this reason, the closure problems required to evaluate the model parameters are all Stokes-like (as presented in Section 2.2). We anticipate at this stage that an alternative, modified approach in which the upscaled coefficients are sensitive to near-wall advection will be introduced in Section 3.2. Finally, it is noteworthy that the effective boundary conditions (Eqs. (4)–(6)) were formulated in Refs. [16,20] considering the simple case of a surface/substrate for which the coordinates ($\hat{x}$, $\hat{y}$, $\hat{z}$) are the principal axes of the Navier-slip tensor.

2.2. Evaluation of the macroscopic coefficients

In order to evaluate the dimensionless macroscopic coefficients for different surface textures, the closure problems derived in Refs. [16,20] are employed here, and the Stokes-based approach proposed for the calculation of the model parameters is adopted. The closure problems are solved over an elementary cell, representative of the microscopic domain of interest, with the dimensions normalized by the microscopic length scale ℓ; the dimensionless coordinates $x_i = \hat{x}_i/\ell$ used to describe the closure fields are shown in the right frame of Fig. 1.

For the Navier-slip (λ_x, λ_z) and interface permeability ($\mathcal{K}^{itf}_{xy}$, $\mathcal{K}^{itf}_{zy}$) coefficients, it is sufficient to solve two Stokes-like systems governing the auxiliary variables ($u^\dagger_{11}$, $u^\dagger_{21}$, $u^\dagger_{31}$, $p^\dagger_1$) and ($u^\dagger_{13}$, $u^\dagger_{23}$, $u^\dagger_{33}$, $p^\dagger_3$), which stem from the homogenization procedure, over the microscopic elementary cell, subject to periodicity of all the dependent variables in the x and z directions; the two systems are defined, respectively, as follows:

$$\begin{cases} \partial_i u^\dagger_{i1} = 0, \\ -\partial_i p^\dagger_1 + \partial^2_k u^\dagger_{i1} = 0, \\ u^\dagger_{i1} = 0 \quad \text{at } \mathcal{I}_{\beta\sigma}, \\ -p^\dagger_1 \delta_{i2} + \partial_2 u^\dagger_{i1} + \partial_i u^\dagger_{21} = \delta_{i1} \quad \text{at } y = y_\infty, \end{cases} \tag{9}$$

and

$$\begin{cases} \partial_i u^\dagger_{i3} = 0, \\ -\partial_i p^\dagger_3 + \partial^2_k u^\dagger_{i3} = 0, \\ u^\dagger_{i3} = 0 \quad \text{at } \mathcal{I}_{\beta\sigma}, \\ -p^\dagger_3 \delta_{i2} + \partial_2 u^\dagger_{i3} + \partial_i u^\dagger_{23} = \delta_{i3} \quad \text{at } y = y_\infty, \end{cases} \tag{10}$$

with the operators $\partial_i = \frac{\partial}{\partial x_i}$ and $\partial^2_i = \frac{\partial^2}{\partial x^2_i}$, and δ_{ij} the Kronecker delta function. $\mathcal{I}_{\beta\sigma}$ refers to the physical interface between the fluid phase (β) and the ribs/grains/solid walls (σ). Systems (9) and (10) must be solved for a sufficiently large value of $y_\infty = \hat{y}_\infty/\ell$ so that the microscopic fields are homogeneous in x and z near the matching interface. Once the closure fields are available by performing simple numerical simulations with y_∞ set, for instance, to 5 (which is common practice), the macroscopic coefficients for a matching interface of particular interest at $y_\infty = 0$ can be directly evaluated, without having to rerun the simulations; they can be calculated as follows [16–18]:

$$\lambda_x = \frac{1}{\mathcal{A}} \int_{S_0} u^\dagger_{11} \, dA, \quad \lambda_z = \frac{1}{\mathcal{A}} \int_{S_0} u^\dagger_{33} \, dA, \tag{11}$$

$$\mathcal{K}^{itf}_{xy} = \frac{1}{\mathcal{A}} \int_{\mathcal{V}_0} u^\dagger_{11} \, dV, \quad \mathcal{K}^{itf}_{zy} = \frac{1}{\mathcal{A}} \int_{\mathcal{V}_0} u^\dagger_{33} \, dV, \tag{12}$$

where S_0 and $\mathcal{V}_0$ are the virtual surface at and the fluid volume below the plane $y = 0$, respectively, and $\mathcal{A}$ is the area of an $x-z$ cross section of the elementary cell (if the surface texture has a fixed dimensional pitch, ℓ, in both $\hat{x}$ and $\hat{z}$, then $\mathcal{A} = 1 \times 1$).

For the medium permeability component $\mathcal{K}_{yy}$, a triply periodic unit cell of the porous region is considered, and the following closure system
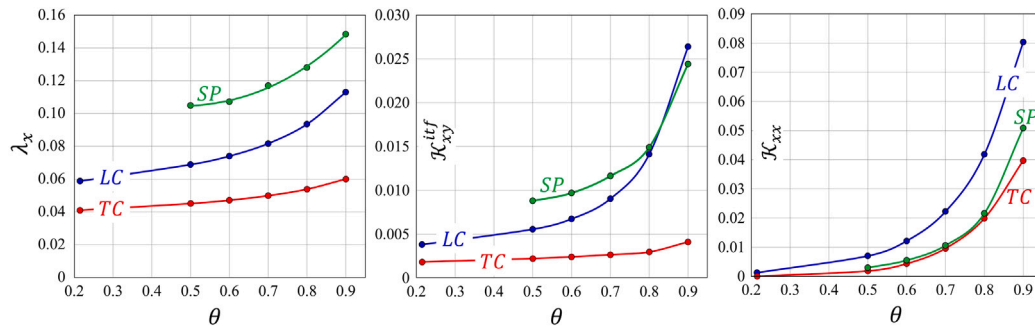
---

[1] The porosity θ of a permeable medium is defined as the ratio of the volume occupied by the pores to the total volume of the medium.

Fig. 2. Graphical representation of the results in Table 1.

Table 1

Dependence of the macroscopic coefficients (Navier-slip, λ_x, interface permeability, $\mathcal{K}_{xy}^{itf}$, and medium permeability, $\mathcal{K}_{xx}$) on porosity, θ, for substrates consisting of inline (i) longitudinal, X-elongated cylinders (LC), (ii) transverse, Z-elongated cylinders (TC), and (iii) spheres (SP).

Porosity	λ_x ($\times10^{-2}$)			$\mathcal{K}_{xy}^{itf}$ ($\times10^{-2}$)			$\mathcal{K}_{xx}$ ($\times10^{-2}$)		
(θ)	LC	TC	SP	LC	TC	SP	LC	TC	SP
0.215	5.88	4.10	–	0.38	0.18	–	0.12	0	–
0.5	6.88	4.51	10.49	0.56	0.22	0.88	0.70	0.18	0.30
0.6	7.40	4.71	10.72	0.67	0.24	0.97	1.21	0.43	0.55
0.7	8.17	4.99	11.70	0.90	0.27	1.16	2.22	0.96	1.06
0.8	9.35	5.39	12.81	1.41	0.30	1.49	4.18	1.99	2.16
0.9	11.30	6.01	14.84	2.64	0.41	2.44	8.03	3.97	5.08

Table 2

Values of the macroscopic coefficients for surfaces roughened with (i) longitudinal square ribs (LSQ), (ii) transverse square ribs (TSQ), (iii) longitudinal semicircular elements (LSC), (iv) transverse semicircular elements (TSC), and (v) inline array of cubic elements (CU), at different values of the rib height-to-pitch ratio, e/ℓ.

e/ℓ	λ_x ($\times10^{-2}$)					$\mathcal{K}_{xy}^{itf}$ ($\times10^{-2}$)				
	LSQ	TSQ	LSC	TSC	CU	LSQ	TSQ	LSC	TSC	CU
0.05	4.22	3.67	4.22	3.79	4.90	0.10	0.09	0.10	0.09	0.12
0.10	6.95	5.06	6.96	5.50	9.09	0.34	0.23	0.32	0.24	0.45
0.15	8.40	5.09	8.42	5.86	12.02	0.60	0.30	0.56	0.33	0.87
0.20	8.86	4.57	8.90	5.65	13.29	0.82	0.29	0.72	0.34	1.26
0.25	8.61	3.98	8.72	5.33	13.34	0.96	0.23	0.79	0.31	1.49
0.30	7.92	3.46	8.17	5.02	12.46	1.00	0.17	0.76	0.28	1.57
0.40	6.02	2.59	6.88	4.53	9.50	0.86	0.08	0.55	0.22	1.28
0.50	4.16	1.78	5.88	4.10	6.47	0.58	0.04	0.38	0.18	0.83

is solved over it, with the free index j set to 2:

$$\begin{cases} \partial_i \breve{u}_{ij} = 0, \\ -\partial_i \breve{p}_j + \partial_k^2 \breve{u}_{ij} = -\delta_{ij}, \\ \breve{u}_{ij} = 0 \qquad \text{at } \mathcal{I}_{\beta\sigma}, \end{cases} \qquad (13)$$

subject to periodicity of $\breve{u}_{ij}$ and $\breve{p}_j$ in x, y and z. The $\breve{u}_{22}$ field is then superficially averaged over the volume of the unit cell to evaluate the coefficient $\mathcal{K}_{yy}$. Should the medium permeability components $\mathcal{K}_{xx}$ or $\mathcal{K}_{zz}$ be needed (although they do not contribute to the effective boundary conditions), system (13) is to be solved for j equal to 1 or 3, respectively, and the superficial averaging is to be applied considering, respectively, $\breve{u}_{11}$ or $\breve{u}_{33}$. For the case of a corrugated, impermeable boundary, it is clear that $\mathcal{K}_{ii}$ vanishes identically, while the interface permeability coefficients do not.

Numerical values of the macroscopic coefficients entering the effective boundary conditions at the virtual interface for selected configurations of porous or rough layers are listed, respectively, in Tables 1 and 2; their behaviors with variations in the porosity (θ) for the different permeable beds and in the rib size-to-pitch ratio (e/ℓ) for the rough surfaces are correspondingly plotted in Figs. 2 and 3. The values reported are either evaluated through this work (for spherical grains, longitudinal/transverse ribs of semicircular cross sections, and cubic roughness elements) or gathered from the literature (for streamwise/spanwise cylinders [20] and ribs of square cross sections [18]). For the case of longitudinal (respectively transverse) solid inclusions/ribs, values of the coefficients λ_z, $\mathcal{K}_{zy}^{itf}$ and $\mathcal{K}_{zz}$ can be inferred, although they are not explicitly given in the tables, since they are equal to λ_x, $\mathcal{K}_{xy}^{itf}$ and $\mathcal{K}_{xx}$ of the transverse (respectively longitudinal) case at the same value of θ or e/ℓ. When the cylindrical inclusions are elongated in the spanwise (z) or in the streamwise (x) direction, the medium permeability component $\mathcal{K}_{yy}$ is the same (for given porosity) and is equal to $\mathcal{K}_{xx}$ for the case of transverse cylinders (which coincides with $\mathcal{K}_{zz}$ for longitudinal ones). For isotropic patterns such as porous substrates made of ordered spherical grains, it is clear that $\lambda_x = \lambda_z$, $\mathcal{K}_{xy}^{itf} = \mathcal{K}_{zy}^{itf}$, and $\mathcal{K}_{xx} = \mathcal{K}_{yy} = \mathcal{K}_{zz}$. Although the medium permeability component $\mathcal{K}_{xx}$ (and $\mathcal{K}_{zz}$) does not contribute to the homogenized, effective boundary conditions, its

values are presented for permeable beds in Table 1 to highlight the difference with respect to the corresponding interface permeability $\mathcal{K}_{xy}^{itf}$ (also $\mathcal{K}_{zy}^{itf}$). For the rough walls considered, the macroscopic coefficients of interest exhibit non-monotonic relationships with the rib size-to-pitch ratio (Fig. 3), where they all peak within the range $0.1 \lesssim e/\ell \lesssim 0.3$. This behavior is not unexpected, since the model coefficients vanish for cubic or longitudinal/transverse square ribs as e/ℓ tends to 0 or 1, when the smooth surface case is recovered.

3. The macroscale problem: case studies, validation and discussion

3.1. Laminar poiseuille flow in rough/permeable channels

3.1.1. A generalized analytical solution

The problem of laminar, pressure-driven flow in a channel bounded by stationary rough/permeable layers at $\hat{y} < 0$ and $\hat{y} > 2H$ is studied here in pursuit of a generalized analytical solution for the macroscopic velocity profile across the free-fluid region (cf. Fig. 4).

First, we seek dimensionless expressions of the governing Eqs. (3) pertinent to the macroscale problem. With $\mathcal{M}$ the magnitude of the pressure gradient forcing the channel flow in the streamwise direction, a bulk stress/pressure scale may be defined as $\tau^{\mathcal{M}} = \mathcal{M}H$. The velocity scale is chosen as $u_\tau = \sqrt{\tau^{\mathcal{M}}/\rho}$, corresponding to a shear velocity. The dimensionless macroscopic variables are introduced as follows:

$$X_i = \frac{\hat{x}_i}{H}, \quad U_i = \frac{\hat{u}_i}{u_\tau}, \quad P = \frac{\hat{p}}{\mathcal{M}H}, \qquad (14)$$

for the normalized pressure gradient to become $\partial P/\partial X = -1$. The $X - Z$ planform of the near-wall micro-patterns is assumed to be either isotropic or elongated in the spanwise or streamwise direction; in this case, there are no near-wall transverse velocity components [21] and the fully developed flow is oriented only along X, i.e. $U = U(Y)$ and $V = W = 0$. Substituting (14) into (3) we obtain the following dimensionless conservation equation governing the macroscale behavior of
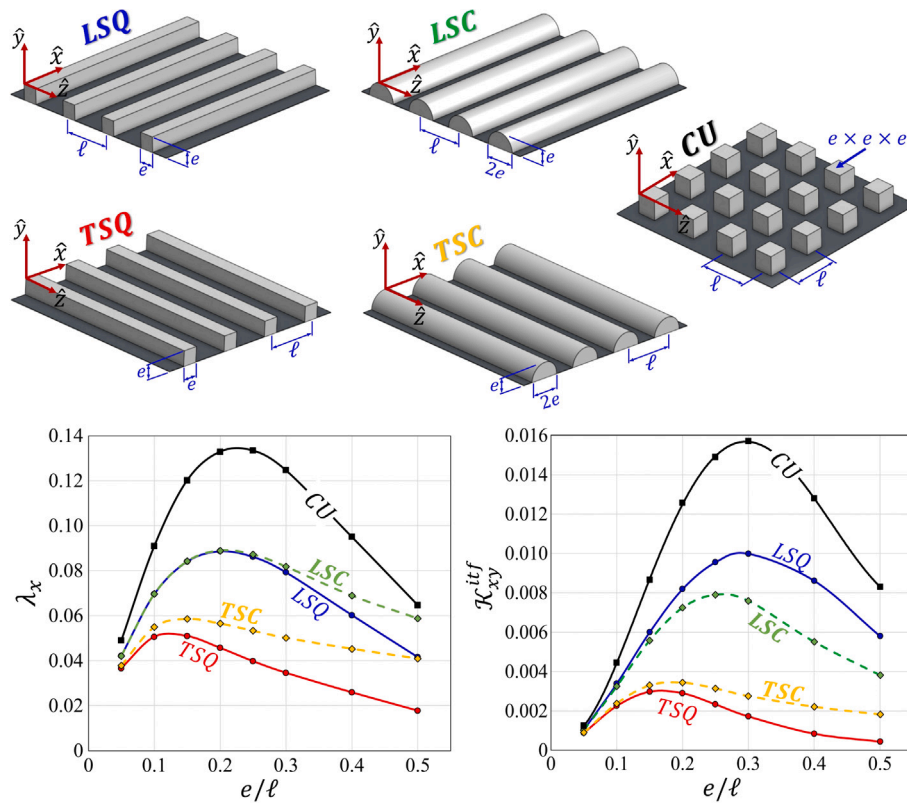
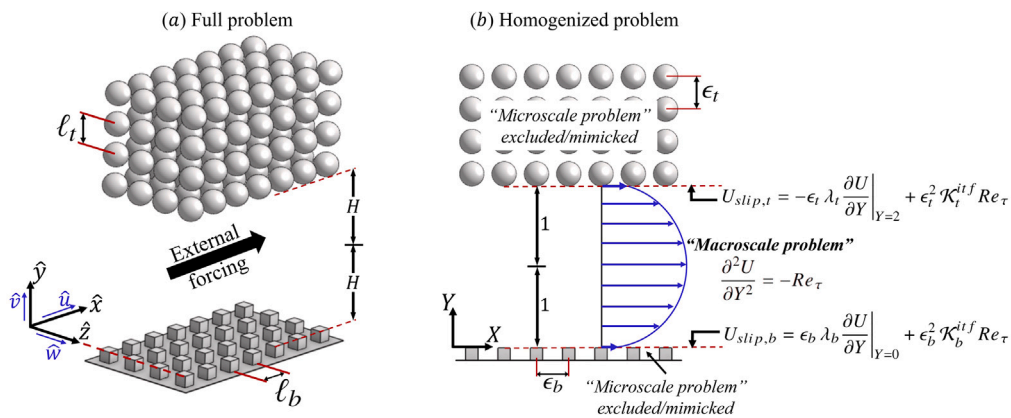**Fig. 3.** Graphical representation of the geometries and results in Table 2.

Fig. 4. Description of the generalized Poiseuille flow problem, with examples of the rough/permeable walls: (*a*) sketch of the full problem in dimensional coordinates; (*b*) sketch of the homogenized problem in dimensionless macroscopic coordinates, with the governing equation and the effective boundary conditions explicitly indicated.

the flow:

$$\frac{\partial^2 U}{\partial Y^2} = -Re_\tau, \tag{15}$$

where $Re_\tau = \dfrac{\rho u_\tau H}{\mu}$ corresponds to a shear-velocity Reynolds number. A general solution of Eq. (15) is

$$U(Y) = Re_\tau \left[-\frac{Y^2}{2} + (1 - A)Y + B \right], \tag{16}$$

with A and B integration constants. Unlike the case of classical plane Poiseuille flow, A and B do not vanish and can be found from application of the effective boundary conditions which read:

$$U_{slip,b} = U\big|_{Y=0} = \epsilon_b \, \lambda_b \, \frac{\partial U}{\partial Y}\bigg|_{Y=0} + \epsilon_b^2 \, \mathcal{K}_b^{itf} \, Re_\tau, \tag{17}$$

$$U_{slip,t} = U\big|_{Y=2} = -\epsilon_t \, \lambda_t \, \frac{\partial U}{\partial Y}\bigg|_{Y=2} + \epsilon_t^2 \, \mathcal{K}_t^{itf} \, Re_\tau. \tag{18}$$

Notice that a single coordinate system has been used here, with $X = X_b$ and likewise for Y and Z. The constants A and B are found to be:

$$A = \frac{\Lambda_b (1 + \phi_b) - \Lambda_t (1 + \phi_t)}{2 + \Lambda_b + \Lambda_t}, \quad B = \Lambda_b \frac{\Lambda_t (1 + \phi_t) + (2 + \Lambda_t)(1 + \phi_b)}{2 + \Lambda_b + \Lambda_t}, \tag{19}$$

with the definitions $\Lambda_{b(t)} = \epsilon_{b(t)} \lambda_{b(t)}$ and $\phi_{b(t)} = \epsilon_{b(t)} \dfrac{\mathcal{K}_{b(t)}^{itf}}{\lambda_{b(t)}}$. The slip velocities at the virtual interfaces are

$$U_{slip,b} = B \, Re_\tau, \quad U_{slip,t} = (B - 2A) \, Re_\tau. \tag{20}$$

Eqs. (20) show that the slip speed at each boundary is sensitive to the macroscopic coefficients of both walls. Eq. (16) can now be recast in the following form:

$$U(Y) = -\frac{Re_\tau}{2} Y^2 + \left(Re_\tau + \frac{U_{slip,t} - U_{slip,b}}{2} \right) Y + U_{slip,b}. \tag{21}$$

The position Y_m where the speed is the largest, and the corresponding value of the velocity, $U_{max} = U(Y = Y_m)$, are, respectively,

$$Y_m = 1 + \frac{U_{slip,t} - U_{slip,b}}{2Re_\tau}, \quad U_{max} = \frac{Re_\tau}{2} \left(1 + \frac{U_{slip,t} - U_{slip,b}}{2Re_\tau} \right)^2 + U_{slip,b}, \tag{22}$$

which means that for the *generalized Poiseuille* flow the plane $Y = Y_m$ shifts from the middle section ($Y = 1$) towards the boundary of larger slip, and the maximum velocity, U_{max}, is always larger than the corresponding value in a smooth channel by

$$\Delta U_{max} = \frac{U_{slip,t} + U_{slip,b}}{2} + \frac{1}{8Re_\tau} \left(U_{slip,t} - U_{slip,b} \right)^2. \tag{23}$$

In addition, the bulk, channel-averaged velocity, U_{ch}, deviates from the value for a classical Poiseuille flow by an amount directly proportional to the average of the two slip velocities; such a deviation and its percentage can be expressed as follows:

$$\Delta U_{ch} = \frac{U_{slip,b} + U_{slip,t}}{2}, \quad \Delta U_{ch}\% = 3 \left(\frac{U_{slip,b} + U_{slip,t}}{2 Re_\tau} \right) \times 100\%. \tag{24}$$

Finally, if the boundary conditions (17) and (18) were only first-order accurate, all the relations derived would hold, except for setting ϕ_b and ϕ_t to 0 in (19).

3.1.2. Sample validation

Focus shifts now on validating the analytical solution, assessing its applicability range and highlighting its practical relevance. We define the bulk Reynolds number as $Re = \rho \hat{u}_{ch} H/\mu$, with $\hat{u}_{ch}$ the dimensional channel-averaged velocity. Since $\hat{u}_{ch} = u_\tau U_{ch}$ as per the normalization adopted, the bulk Reynolds number is also $Re = U_{ch} Re_\tau$. For a smooth, impermeable channel, it is $U_{ch} = Re_\tau/3$, hence $Re_\tau = \sqrt{3 Re}$. With a transitional Re of order 1000 for the classical plane Poiseuille flow [22, 23], the flow is expected to remain laminar until Re_τ of order 50. For all the cases discussed in this section, Re_τ is well below this threshold, typically $Re_\tau \leq 10$. The performance of the rough/permeable channels and the smooth ones are compared at a fixed Re_τ, i.e. at a fixed applied pressure gradient. Validation of the model requires conducting full Navier–Stokes simulations in a channel of length L_X, with all fields near and within the corrugations/pores of the surfaces/substrates well resolved. The length of the channel was progressively increased and dependency of the computed X-Z-averaged streamwise velocity on it was monitored; for the configurations/conditions considered here, it was proven that a single geometrically periodic cell of the channel is sufficient to apply periodicity of the fields and, thus, to fully describe the channel flow, which implies the absence of any flow instabilities such as vortex shedding in the vicinity of the roughness elements/grains (the reader is encouraged to refer to Ref. [24] for a relevant description). Then, the velocity profile across the channel, constructed by evaluating the plane-averaged value of the streamwise velocity U at each wall-normal distance Y, was compared to the analytical solution (Eq. (21)). All simulations were run using Simcenter STAR-CCM+ finite-volume-based software (versions 16.02.009-R8 and 18.02.008-R8).

Three types of bounding walls are involved in the validation step. First, smooth, impermeable surfaces (SM) having $\lambda = \mathcal{K}^{itf} = 0$. Second, surfaces roughened by transverse, Z-elongated, square elements of a rib size-to-pitch ratio $e/\ell = 0.25$ ($\lambda = 0.03975$ and $\mathcal{K}^{itf} = 0.00233$; cf. Table 2), with $\epsilon = \ell/H = 0.4$ or 0.8. Such surfaces are indicated as $SQ_\epsilon^{e/\ell}$, i.e., $SQ_{0.4}^{0.25}$ and $SQ_{0.8}^{0.25}$. Third, fluid-saturated porous substrates formed by transverse cylindrical inclusions, with porosity $\theta = 0.8$

($\lambda = 0.05385$ and $\mathcal{K}^{itf} = 0.00297$; cf. Table 1), with $\epsilon = \ell/H = 0.4$ or 0.8. These substrates are referred to as TC_ϵ^θ, i.e., $TC_{0.4}^{0.8}$ and $TC_{0.8}^{0.8}$. To provide extensive validation of the model predictions, six combinations of the aforementioned walls were selected, as illustrated in Fig. 5 with indication of the values of Λ and ϕ for each boundary and the integration constants A and B for each channel. The macroscopic velocity profiles, based on Eq. (16), are in perfect agreement with results of the full simulations. The errors in the model predictions for the slip velocities, ΔU_{max} and ΔU_{ch} (cf. Eqs. (20), (23) and (24), respectively) are within about $\pm 3\%$. Since results of the first- and the second-order models are indistinguishable from one another to graphical accuracy, only the predictions of the latter are plotted in the figure.

3.1.3. Considerations on model accuracy

The applicability of the effective boundary conditions depends on the separation of scales between the microscopic and the macroscopic problems, with the accuracy of the model expected to degrade at large values of the ratios ϵ_b and ϵ_t. This may be associated with enhanced near-wall advection as the streamlines deflect due to the dynamic interaction of the fluid with surface protrusions; such inertial effects cannot be predicted by the Stokes-like systems underlying the homogenization procedure. Porous substrates ($\theta = 0.8$) formed by either spanwise- or streamwise-elongated cylinders are chosen here as representative examples, to highlight how errors in the model predictions increase with ϵ, as shown in Fig. 6. It is clear that even the second-order accurate interface condition does not guarantee high accuracy for the case of transverse cylinders when ϵ is sufficiently large (*cf.* Fig. 6, right). By contrast, if the cylinders are aligned along X, interaction with the bulk channel flow is simply in the form of a skin-friction force, with negligible inertial effects; this justifies the perfect agreement in Fig. 6 between the second-order macroscopic solution and the results of the full simulations. It is noteworthy that the slip and the bulk velocities are larger for the case of longitudinal cylinders since the macroscopic coefficients ($\lambda = 0.09347$ and $\mathcal{K}^{itf} = 0.01410$) are larger than for the transverse cylinders configuration at the same porosity ($\lambda = 0.05385$ and $\mathcal{K}^{itf} = 0.00297$; cf. Table 1).

3.1.4. Random media

Channels delimited by porous substrates/structured surfaces formed by random patterns of inclusions/roughness elements represent a more practical situation. The homogenization approach applies to such configurations provided that a sufficiently large microscopic elementary volume is chosen to represent the features of the whole media/surface. An example is shown in Fig. 7; the permeable bed, bounding the flow from the upper side, consists of 100 Z-elongated inclusions, randomly displaced in the $X - Y$ plane, with overlapping allowed among neighboring grains. On average, there are 20 grains along X and 5 grains in Y; the diameters of the inclusions are varied, for the porosity to fluctuate locally between 0.25 and 0.75, yielding an average porosity $\theta_{avr} \approx 0.5$. The microscopic length scale, ℓ_t, was chosen as $L_X/20$, with $L_X = 4 H$ the length of the periodic domain selected; hence, it can be concluded that $\epsilon_t = \ell_t/H = 0.2$. The microscale problem was approached in the same manner as that followed by Naqvi & Bottaro [16] for a random medium, and the coefficients were evaluated to be $\lambda_t = 0.1012$ and $\mathcal{K}_t^{itf} = 0.0112$ ($\Lambda_t = 0.0202$ and $\phi_t = 0.0221$). The macroscopic velocity profile, based on the analytical solution (16), matches well the streamwise-averaged results from the full simulation, cf. Fig. 7.

3.1.5. Three-dimensional patterns

Until this point, validation of the model has been sought only for two-dimensional configurations of rough/porous walls. However, as mentioned in Section 3.1.1, a macroscopically one-directional flow is also expected over three-dimensional patterns provided that the external forcing (here in X) is aligned with one of the principal axes of the Navier-slip tensor. An example is illustrated in Fig. 8, where channel
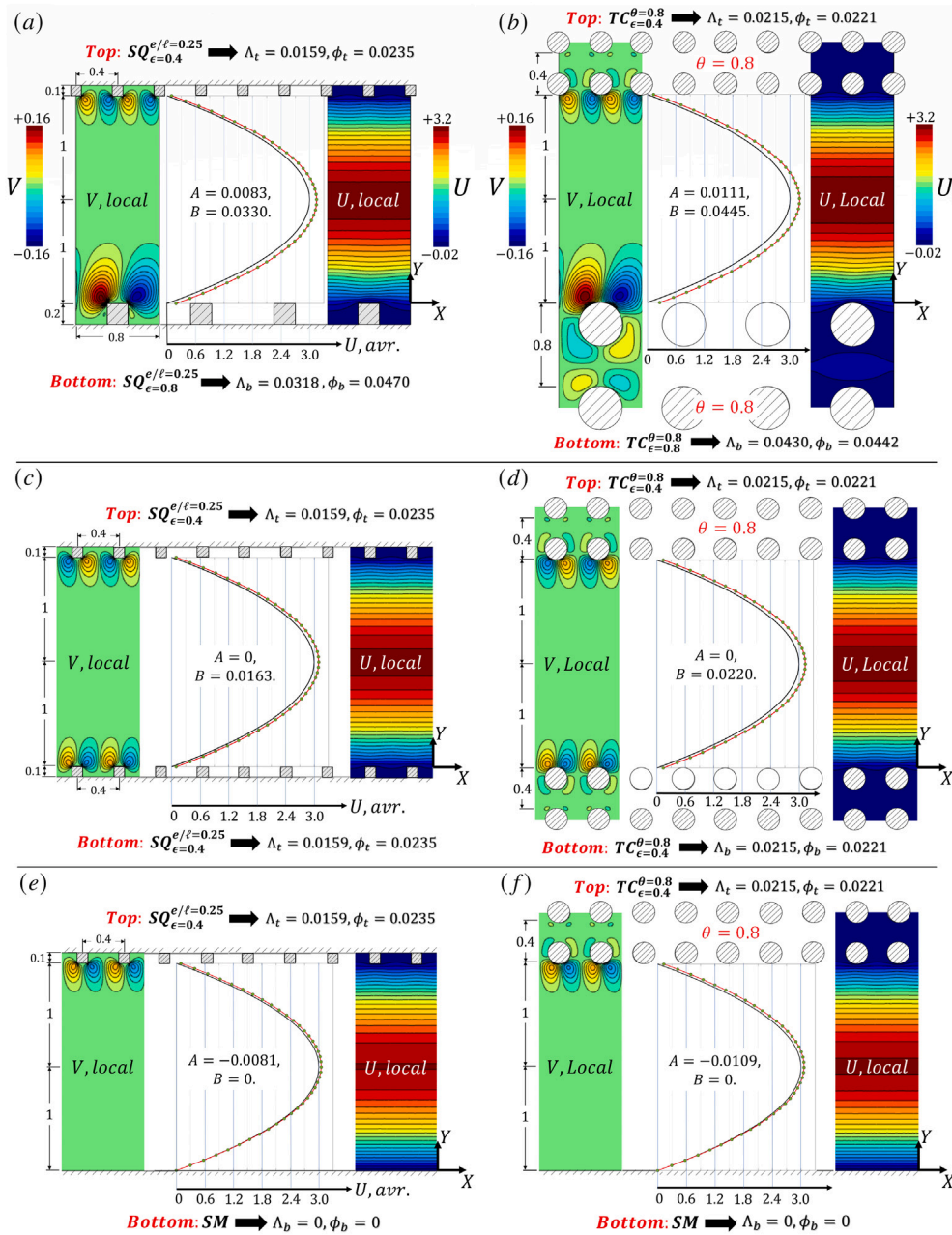
Fig. 5. Laminar flow ($Re_\tau = 6$) in asymmetric rough (a) or permeable (b) channels, symmetric rough (c) or permeable (d) channels, and channels bounded by a smooth surface from one side and a rough surface (e) or a porous substrate (f) from the other side. The analytical results (second-order) for the velocity profiles (red lines) are validated by plane-averaged values from the full simulations (green-filled circles); the black profiles refer to Poiseuille flow in a smooth, impermeable channel, for which $A = B = 0$.
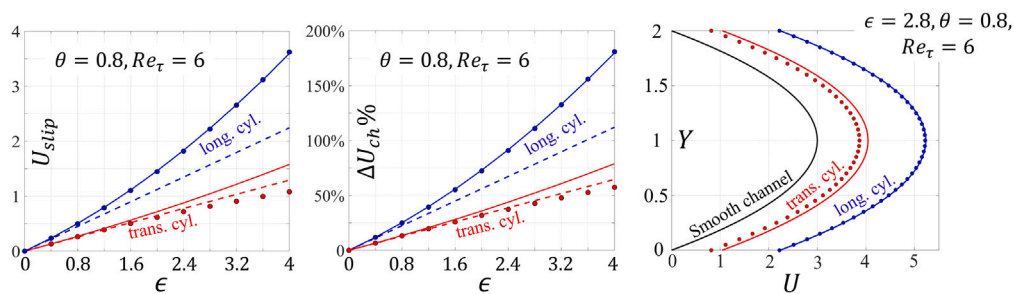
Fig. 6. Laminar flow ($Re_\tau = 6$) in symmetric channels bounded by porous substrates consisting of either transverse or longitudinal cylinders, with porosity $\theta = 0.8$. The analytical results (dashed lines: first-order; solid lines: second-order) are compared with results of the full simulations (filled circles).
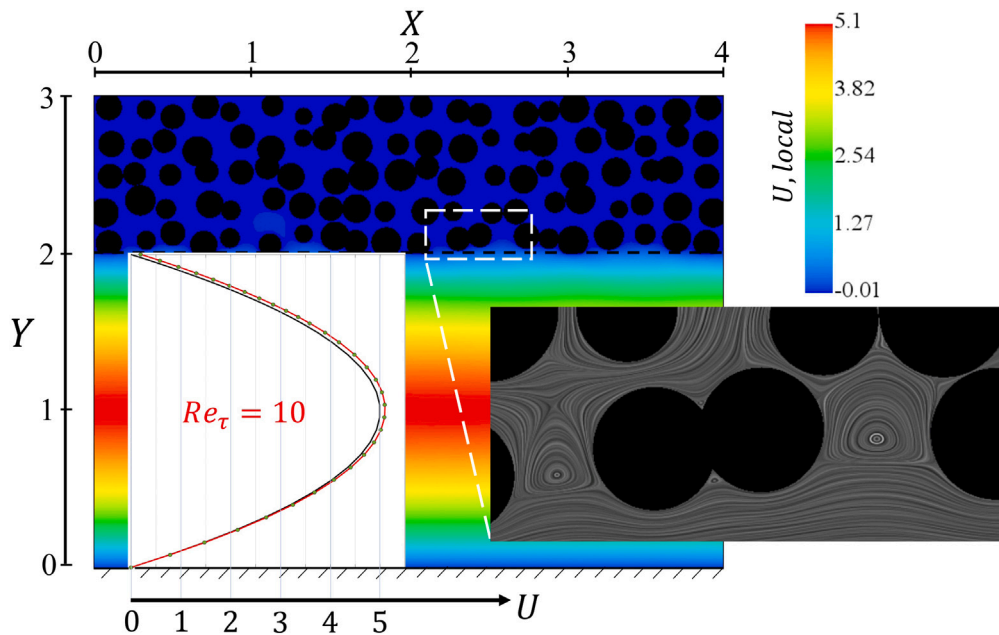
Fig. 7. Laminar flow ($Re_\tau = 10$) in a channel bounded from the top by a porous layer consisting of randomly arranged, spanwise-aligned inclusions, with the average porosity equal to 0.5. A close-up of the velocity vector field near the interface (visualized via the line integral convolution method) is displayed in the gray frame. Analytical solution for the upscaled velocity profile is validated against the full simulation; symbols are identical to those in Fig. 5.
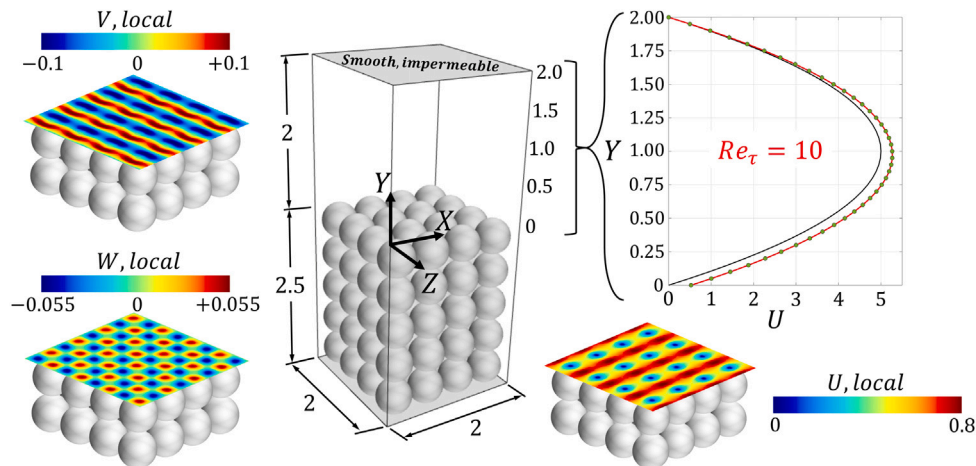

Fig. 8. Laminar flow ($Re_\tau = 10$) in a channel bounded on the lower side by a porous bed consisting of inline spheres, with $\theta = 0.5$ ($\lambda_b = 0.1049$ and $\mathcal{K}_b^{itf} = 0.0088$; cf. Table 1) and $\epsilon = 0.5$. On the top right image, the analytical solution for U is plotted together with results from the full simulation, using the same symbols as in Fig. 5.

flow over a porous substrate consisting of aligned spherical grains is analyzed. Distributions of the three velocity components at the virtual interface ($Y = 0$) are displayed to confirm that, consistently with the aforementioned condition, the plane-averaged values of wall-normal and spanwise velocity components vanish; the analytical prediction of the streamwise velocity agrees very well with the X-Z-averaged result from the three-dimensional, feature-resolving simulation.

3.1.6. Small roughness/grains amplitudes

A simplified version of the *generalized Poiseuille* solution is proposed for laminar flows in channels bounded by walls of small roughness amplitude or by permeable layers with reduced dimensions of grains and pores. In these cases, ϵ is sufficiently small and we expect the hierarchy $\epsilon^2 \mathcal{K}^{itf} \ll \epsilon\lambda \ll 1$ to hold. This permits not only to safely reduce the model to first order (by neglecting ϕ in (19)) but also to use the approximation $1 + \Lambda \approx 1$ when evaluating the different parameters

of interest; for instance, we obtain

$$U_{slip,b(t)} = Re_\tau \, \Lambda_{b(t)}, \quad \Delta U_{max} = Re_\tau \frac{\Lambda_b + \Lambda_t}{2}, \quad \Delta U_{ch}\% = 3 \frac{\Lambda_b + \Lambda_t}{2} \times 100\%. \tag{25}$$

The simplified solution is validated in Fig. 9 for the flow in a channel bounded on the top by a porous substrate of porosity equal to 0.5, for ϵ ranging from 0 to 0.8. For all types of porous inclusions considered, a linear behavior of $U_{slip,t}$, U_{max} and $\Delta U_{ch}\%$ is found versus ϵ, and the first-order boundary condition yields excellent predictions.

3.2. A crash introduction to the near-wall advection modeling

In the original structure of the homogenization model, described in Section 2 and validated in Section 3.1, inertial effects are absent from the problems at the two leading orders in ϵ, and the microscopic systems of equations are Stokes-like. Nevertheless, as anticipated in
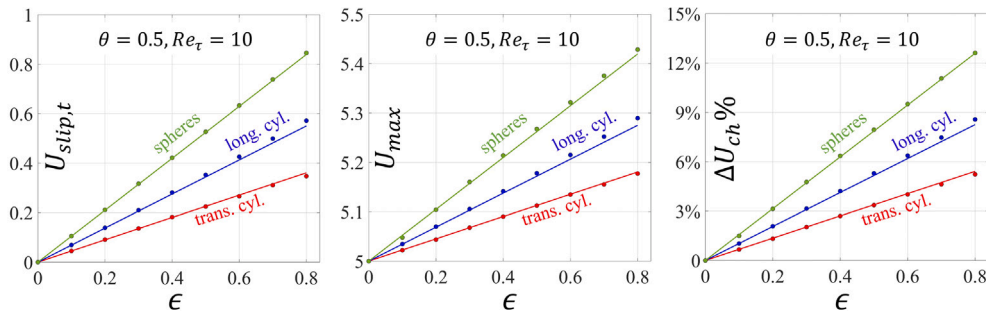
Fig. 9. Laminar flow ($Re_\tau = 10$) in a channel bounded on one side by a smooth wall and on the other side by a porous substrate ($\theta = 0.5$) consisting of either spheres ($\lambda = 0.1049$), longitudinal cylinders ($\lambda = 0.0688$), or transverse cylinders ($\lambda = 0.0451$). The simplified solution (lines) is validated against full simulations (filled circles).

Section 3.1.3, near-wall advection may contribute significantly to the problem at relatively large values of ϵ, limiting the validity range of the upscaling model adopted. In this section, we propose (and then validate) an adjustment to the homogenization procedure such that effects of near-wall advection on the macroscale behavior of the laminar channel flow can be mimicked efficiently.

In the recent study by Ahmed & Bottaro [25], the problem of seepage in porous media beyond the Stokes flow conditions has been treated, and it was proved that the same upscaled governing equation (Darcy's law in that case) still applies, but with the permeability appropriately modified to be dependent on the Reynolds number, deviating from the intrinsic permeability of the medium, which is merely geometry-dependent. The problem under study here is different since flow over, and not through, porous substrates is analyzed. However, an analogous procedure is adopted so that the effective boundary conditions (Eqs. (17) and (18)) and, hence, the generalized solution for the velocity profile across the channel and all the relevant relationships derived in Section 3.1.1, hold at considerably large values of ϵ and/or Re_τ. The auxiliary systems used to evaluate the Navier-slip and the interface-permeability coefficients (respectively, $\lambda_{b(t)}$ and $\mathcal{K}_{b(t)}^{itf}$) are reformulated to properly model the sensitivity of the microscopic fields, and therefore the model coefficients, to near-wall inertia. The general procedure outlined by Buda [26] is followed, with some adjustment, to yield a reliable homogenization framework aimed at genuinely capturing the role of near-interface advection in the *generalized Poiseuille* problem under laminar flow conditions. Extensive validation of the proposed model is subsequently performed for different geometric and flow conditions.

3.2.1. Adjustment of the homogenization model

An Oseen-like linearization was proposed by Buda [26] to try to include the effects of near-interface advection in the homogenization scheme. Accordingly, the convective acceleration terms in the momentum conservation equation governing the microscopic problem were linearized, by defining a constant, spatially invariant, dimensional velocity $\hat{u}_{\phi,i} = (\hat{u}_\phi, 0, 0)$ representative of the velocity level near the physical wall where the inertial effects may be significant as the fluid interacts with the protrusions/grains. Hence, the microscale problem is now governed by the following conservation equations:

$$\frac{\partial \hat{u}_i}{\partial \hat{x}_i} = 0, \quad \rho \hat{u}_{\phi,j} \frac{\partial \hat{u}_i}{\partial \hat{x}_j} = -\frac{\partial \hat{p}}{\partial \hat{x}_i} + \mu \frac{\partial^2 \hat{u}_i}{\partial \hat{x}_j^2}. \tag{26}$$

The microscopic Reynolds number, defined as $Re_\phi = \rho \hat{u}_\phi \ell / \mu$, is now assumed to be of $\mathcal{O}(1)$. By introducing the dimensionless velocity $U_\phi = \dfrac{\hat{u}_\phi}{u_\tau}$, one may write

$$Re_\phi = \frac{\rho \hat{u}_\phi \ell}{\mu} = \frac{\ell}{H} \frac{\rho u_\tau H}{\mu} \frac{\hat{u}_\phi}{u_\tau} = \epsilon Re_\tau U_\phi. \tag{27}$$

A homogenization procedure similar, in principle, to that described in Section 2.1 was then followed by Buda [26]; the same effective

boundary conditions (Eqs. (4)–(6)) were eventually attained, yet the closure problems based on which the macroscopic coefficients are calculated differ from those presented in Section 2.2 and read

$$\begin{cases} \partial_i u_{i1}^\dagger = 0, \\ -\partial_i p_1^\dagger + \partial_k^2 u_{i1}^\dagger = Re_\phi \, \partial_1 u_{i1}^\dagger, \\ u_{i1}^\dagger = 0 \quad \text{at } \mathcal{I}_{\beta\sigma}, \\ -p_1^\dagger \delta_{i2} + \partial_2 u_{i1}^\dagger + \partial_i u_{21}^\dagger = \delta_{i1} \quad \text{at } y = y_\infty. \end{cases} \tag{28}$$

As before, the coefficients λ_x and $\mathcal{K}_{xy}^{itf}$ can be calculated based on the closure variable $u_{11}^\dagger$ as follows:

$$\lambda_x = \frac{1}{\mathcal{A}} \int_{S_0} u_{11}^\dagger \, dA, \quad \mathcal{K}_{xy}^{itf} = \frac{1}{\mathcal{A}} \int_{\mathcal{V}_0} u_{11}^\dagger \, dV, \tag{29}$$

with the same definitions of $\mathcal{A}$, S_0, $\mathcal{V}_0$ given in Section 2.2.

Attention is now drawn to the choice of the characteristic velocity U_ϕ, required for the definition of Re_ϕ which controls the auxiliary system (28). In Ref. [26], the simple assumption $\hat{u}_\phi = u_\tau$ was adopted, and thus $U_\phi = 1$ and $Re_\phi = \epsilon Re_\tau$. Here, a different approach is followed seeking a better approximation for U_ϕ. The velocity level at some normal distance, $\hat{y}_\phi$, away from the effective boundary, located in $\hat{y}_{b(t)} = 0$, is assumed to reasonably characterize near-wall advection; we hypothesize that this distance is proportional to the Navier-slip length $\hat{\lambda}_x$, or simply $\hat{y}_\phi = \hat{\lambda}_x$. In addition, the velocity profile near the boundary is assumed to follow the classical linear relationship

$$U = Y^+ + U_{slip}, \tag{30}$$

with $U = \dfrac{\hat{u}}{u_\tau}$, $Y^+ = \dfrac{\rho u_\tau \hat{y}}{\mu} = \dfrac{\hat{y}}{H} Re_\tau$, and $U_{slip} = \epsilon Re_\tau \lambda_x$ (as per the approximation in Eq. (25)). At $\hat{y} = \hat{\lambda}_x = \ell \lambda_x$, we obtain

$$U_\phi = \frac{\ell}{H} \lambda_x Re_\tau + \epsilon Re_\tau \lambda_x = 2\epsilon Re_\tau \lambda_x, \tag{31}$$

and, therefore, $Re_\phi = 2\epsilon^2 Re_\tau^2 \lambda_x$. With the definition of λ_x in Eq. (29), the final form of the closure problem is

$$\begin{cases} \partial_i u_{i1}^\dagger = 0, \\ -\partial_i p_1^\dagger + \partial_k^2 u_{i1}^\dagger = 2\epsilon^2 Re_\tau^2 \left[\dfrac{1}{\mathcal{A}} \displaystyle\int_{S_0} u_{11}^\dagger \, dA \right] \partial_1 u_{i1}^\dagger, \\ u_{i1}^\dagger = 0 \quad \text{at } \mathcal{I}_{\beta\sigma}, \\ -p_1^\dagger \delta_{i2} + \partial_2 u_{i1}^\dagger + \partial_i u_{21}^\dagger = \delta_{i1} \quad \text{at } y = y_\infty, \end{cases} \tag{32}$$

a well-posed system to be solved over a representative elementary cell of the microscopic domain with all the dependent variables periodic in the x and z directions. This system renders the macroscopic parameters λ_x and $\mathcal{K}_{xy}^{itf}$ dependent not only on the geometry of the structured wall/substrate but also on the control parameter ϵRe_τ. The coefficients calculated based on this approach are indicated here as the *"Oseen-based"* coefficients, while those evaluated based on the original, advection-free system (9) are termed as the *"Stokes-based"* coefficients. Clearly, the Oseen-based system reduces to the Stokes' at $\epsilon Re_\tau = 0$ for any surface texture. However, they are also identical at
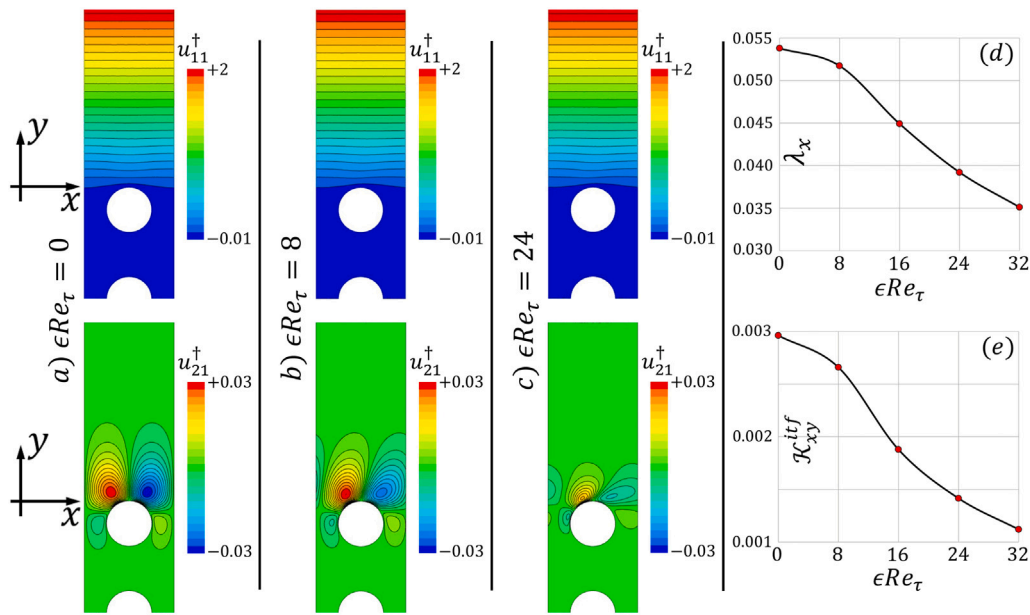
Fig. 10. Contours of the microscopic variables $u_{11}^{\dagger}$ and $u_{21}^{\dagger}$ at three values of ϵRe_{τ}, shown over an x–y plane for the case of spanwise-elongated cylinders of porosity $\theta = 0.8$ (panels a–c). Here, close-ups of the contours near the fluid-porous interface are presented, while in the typical simulations the porous bed ($y < 0$) consists of five rows of cylinders. The Oseen-based macroscopic coefficients λ_x and $\mathcal{K}_{xy}^{itf}$ are plotted in frames (d) and (e) against ϵRe_{τ}.
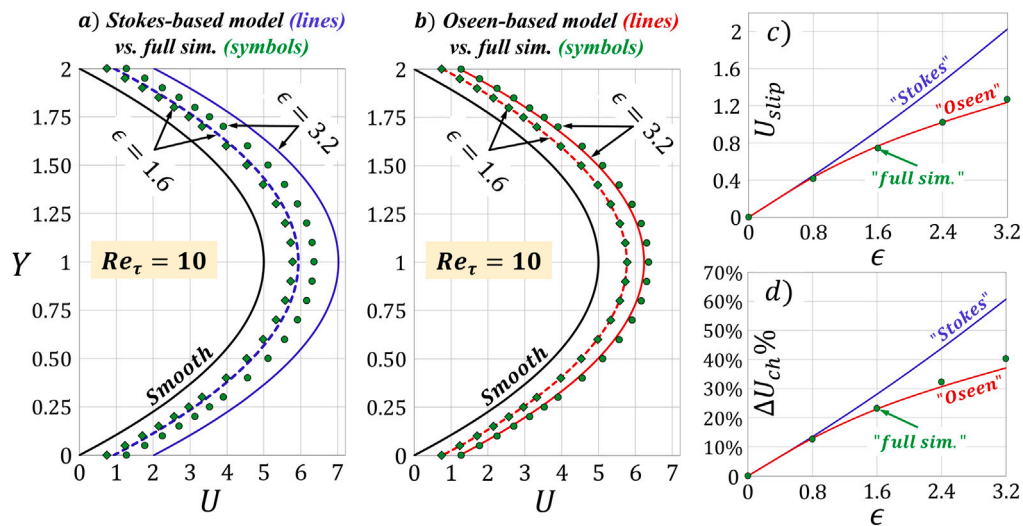

Fig. 11. Poiseuille flow ($Re_{\tau} = 10$) in a channel bounded by two identical porous substrates consisting of inline patterns of spanwise-elongated cylinders ($\theta = 0.8$). Model predictions for the velocity profiles with (a) Stokes-based and (b) Oseen-based macroscopic coefficients are compared against results of the full simulations for two values of ϵ. Corresponding behaviors of (c) U_{slip} and (d) $\Delta U_{ch}\%$ are plotted for ϵ ranging from 0 to 3.2.

finite values of ϵRe_{τ} for the special case of streamwise, x-elongated inclusions/ribs since all the closure variables in the auxiliary system (32) become x_1-invariant, and therefore $\partial_1 u_{i1}^{\dagger}$ vanishes; for this reason, the second-order accurate homogenization model with the Stokes-based coefficients exhibited good accuracy in the case of porous substrates constructed of streamwise-elongated cylinders even at large values of ϵ (in Section 3.1.3), unlike the case of transverse, spanwise-elongated cylinders for which the accuracy deterioration was obvious, and the Oseen-based coefficients should have been used instead, as will be confirmed in Section 3.2.2. In preparation for the upcoming valida-tion step, the configuration of regularly arranged, transversely aligned cylinders with $\theta = 0.8$ was considered for the solution of the closure problem; this provides values of λ_x and $\mathcal{K}_{xy}^{itf}$ for ϵRe_{τ} ranging from 0 to 32, as presented in Fig. 10. It is worth noticing how advection (with the increase of ϵRe_{τ}) distorts the profiles of $u_{21}^{\dagger}$ and reduces the

values of λ_x and $\mathcal{K}_{xy}^{itf}$; for example, at $\epsilon Re_{\tau} = 32$ these two coefficients are lower than their Stokes-based counterparts by about 35% and 62%, respectively (cf. frames (d) and (e)).

3.2.2. Validation and accuracy improvement

Validation of the Oseen-based homogenization approach, described in Section 3.2.1, is performed first on the laminar Poiseuille flow in symmetric channels bounded by permeable beds (porosity $\theta = 0.8$) made of spanwise-elongated cylindrical inclusions in an inline arrange-ment with equal pitch distances ℓ in the $\hat{x}$ and $\hat{y}$ directions. This configuration has been considered earlier, in Section 3.1.3, with the Stokes-based macroscopic coefficients, and deterioration of the model accuracy when proceeding to large values of $\epsilon = \ell/H$, at $Re_{\tau} = 6$, was highlighted and justified. Here, we monitor the improvement in the accuracy of the analytical model when the adjusted coefficients,
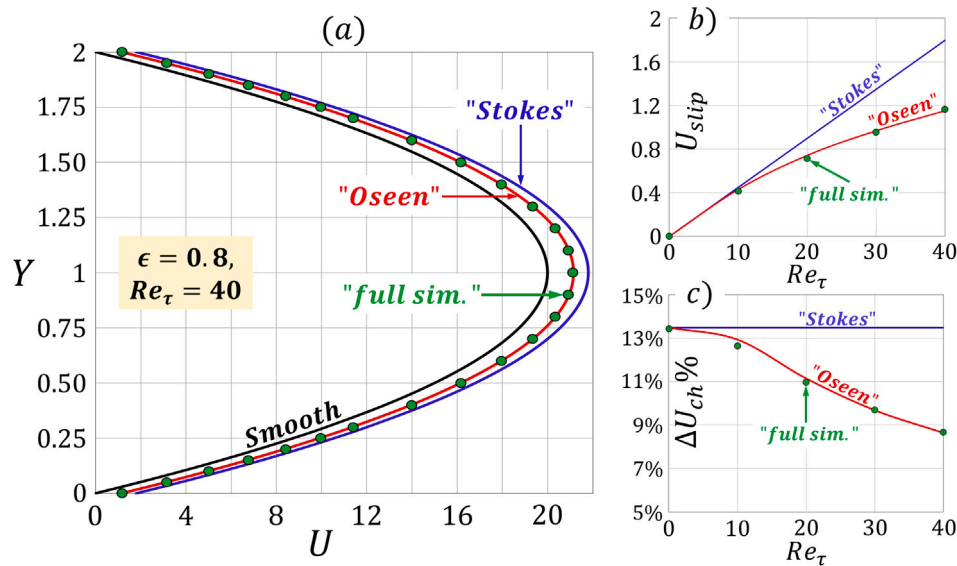
Fig. 12. Poiseuille flow in a channel bounded by two identical porous substrates consisting of inline patterns of spanwise cylinders with $\theta = 0.8$ and $\epsilon = 0.8$. In panel (a), model predictions for the velocity profile using either Stokes-based or Oseen-based macroscopic coefficients are compared against result of the full simulation for $Re_\tau = 40$. Corresponding behaviors of (b) U_{slip} and (c) $\Delta U_{ch}\%$ are plotted with Re_τ varied from 0 to 40.

dependent on the value of ϵRe_τ as plotted in Fig. 10, are plugged into the definition of the constants A and B (Eq. (19)) which control the velocity profile (Eq. (16)). Full, fine-grained simulations were run for values of ϵRe_τ between 0 (Stokes') and 32, either by increasing ϵ from 0 to 3.2 with $Re_\tau = 10$ (presented in Fig. 11) or by increasing Re_τ from 0 to 40 with $\epsilon = 0.8$ (presented in Fig. 12), to provide reference results for validation. From inspection of Figs. 11 and 12, it is evident that predictions of the advection-capturing analytical solution agree very well with results of the feature-resolving simulations. The Stokes-based model overestimates the slip velocity, U_{slip}, at $\epsilon = 3.2$ and $Re_\tau = 10$ by about 60%, while the proposed adjustment is capable of reducing the absolute deviation from the result of the full simulation to less than 3%; cf. Fig. 11(c). This is reflected in more accurate predictions for the percentage change in the channel-averaged velocity due to the presence of the porous substrates, as shown in Fig. 11(d). Similar improvements can be observed in Fig. 12(b) and Fig. 12(c), respectively, as Re_τ increases.

Furthermore, the robustness of the new model has been tested by validating its results for the laminar Poiseuille flow (at $Re_\tau = 12$) in symmetric channels bounded by rough surfaces of different textures. In particular, the boundaries considered are ribbed with transverse elements having square, rectangular, triangular (isosceles), or semicircular cross sections, where $\epsilon = \ell/H = 2$ for all configurations. The geometric characteristics of these patterns (denoted from I to IV), the values of the macroscopic coefficients and the corresponding Stokes- and Oseen-based predictions for the velocity profiles are presented in Fig. 13; the advantage of the Oseen-based approach in enhancing the accuracy of the homogenized model under significant near-wall advection is consistently confirmed.

To facilitate the use of the proposed Oseen-based model in further validation/optimization work, the case of flow over a surface roughened with spanwise-elongated ribs having a square cross section of side length e is considered for a parametric study investigating how the dependence of the Navier-slip and the interface permeability coefficients on the rib size-to-pitch ratio is sensitive to the value of ϵRe_τ, gradually departing from the Stokes flow conditions tested in Ref. [18]. Fig. 14 shows that λ_x and $\mathcal{K}^{itf}_{xy}$ decrease monotonically as ϵRe_τ increases, for all values of e/ℓ, with the coefficients more sensitive to ϵRe_τ within the range $0.1 \leq e/\ell \leq 0.3$.

Finally, it can be concluded from the trends of the macroscopic coefficients, presented in Figs. 10 and 14, and the results for the channel flow, plotted in Figs. 11 and 12, that the Stokes' model is reliable below the threshold $\epsilon Re_\tau \approx 10$, whereas a more versatile homogenization model, which accounts for advection, must be used beyond this limit; the proposed Oseen's linearization is an effective approach to capture this effect.

3.3. What about flow separation?

To investigate the accuracy of the adopted effective boundary conditions in predicting flow separation at the fluid-porous interface, we now consider the combined Couette-Poiseuille laminar flow in a channel bounded from the top (at $\hat{y} = 2H$) by a smooth, impermeable plate moving at a prescribed velocity $\hat{u}_m$ and from the bottom ($\hat{y} < 0$) by a stationary textured wall/substrate, where a fictitious plane interface between the rough/porous layer and the overlying channel flow of interest is chosen at $\hat{y} = 0$; the lower boundary is characterized by dimensionless Navier-slip and interface permeability coefficients, λ and $\mathcal{K}^{itf}$. Besides the motion of the upper plate, a macroscopic pressure gradient $\partial \hat{p}/\partial \hat{x}$ is applied, either favorably or adversely affecting the motion. We define the following dimensionless variables and control parameters:

$$Y = \frac{\hat{y}}{H}, \quad \mathcal{U} = \frac{\hat{u}}{\hat{u}_m}, \quad \mathcal{R} = \frac{H^2}{\mu \hat{u}_m} \frac{\partial \hat{p}}{\partial \hat{x}}, \quad \Lambda = \epsilon \lambda, \quad \phi = \epsilon \frac{\mathcal{K}^{itf}}{\lambda}, \quad (33)$$

where $\mathcal{R} = 0$ characterizes pure Couette flow and $+/-ve$ finite values of $\mathcal{R}$ indicate adverse/favorable pressure gradients, respectively. Under steady, fully developed flow conditions, the following momentum conservation equation governs the problem:

$$\frac{\partial^2 \mathcal{U}}{\partial Y^2} = \mathcal{R}, \quad (34)$$

neglecting advective terms, controlled by the dimensionless parameter $\tilde{\mathcal{R}} = \frac{\rho \hat{u}_m H}{\mu}$. Eq. (34) is subject to the boundary conditions

$$\mathcal{U}\big|_{Y=0} = \Lambda \frac{\partial \mathcal{U}}{\partial Y}\Big|_{Y=0} - \Lambda \phi \mathcal{R}, \quad \mathcal{U}\big|_{Y=2} = 1. \quad (35)$$

The solution of such a *generalized Couette-Poiseuille* problem takes the form

$$\mathcal{U} = \frac{\mathcal{R} Y^2}{2} + \phi \mathcal{R} Y + (Y + \Lambda) \left[\frac{1 - 2\mathcal{R}(1 + \phi)}{2 + \Lambda} \right]. \quad (36)$$
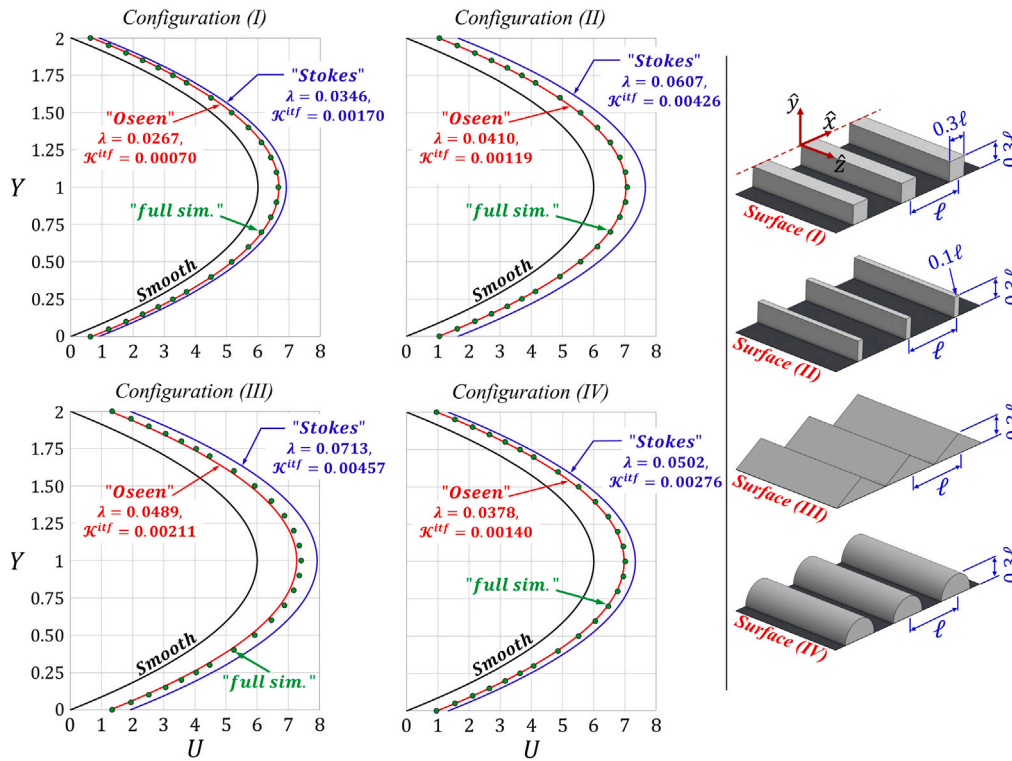
Fig. 13. Poiseuille flow ($Re_\tau = 12$) in symmetric channels bounded by surfaces roughened with spanwise-elongated elements. Four different microstructures of the rough surfaces are considered (cf. the right frame) with $\epsilon = \ell/H = 2$. Model predictions for the velocity profiles (Stokes/Oseen) are compared against results of the full simulations.
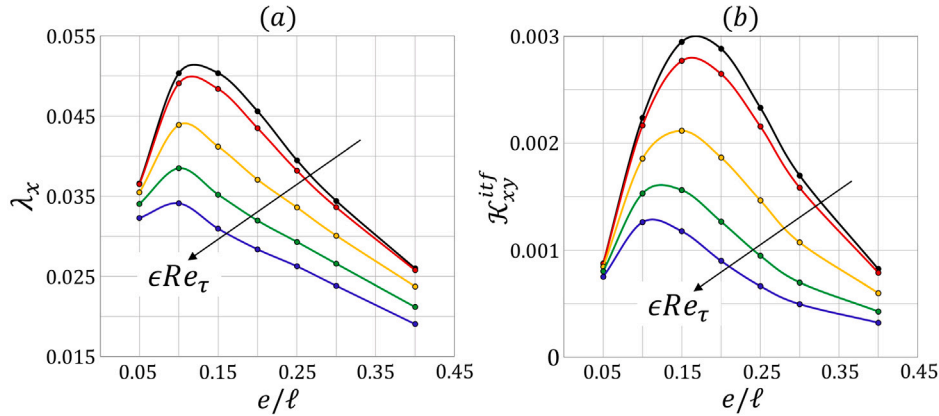

Fig. 14. Surface roughened with transverse square ribs: dependence of λ_x and $\mathcal{K}_{xy}^{itf}$ on the rib size-to-pitch ratio, for ϵRe_τ ranging from 0 (black) to 32 (blue) in steps of 8.

Consequently, the slip velocity at the bottom boundary, $\mathcal{U}_{slip}$, and the bulk, channel-averaged velocity, $\mathcal{U}_{ch}$, read

$$\mathcal{U}_{slip} = \frac{\Lambda}{2+\Lambda}\left[1 - 2\mathcal{R}(1+\phi)\right], \quad \mathcal{U}_{ch} = \left(\frac{2}{3}+\phi\right)\mathcal{R} + \frac{1+\Lambda}{2+\Lambda}\left[1 - 2\mathcal{R}(1+\phi)\right].$$
$$(37)$$

As before, if the boundary condition (35) were first-order accurate, the relations (36) and (37) would hold, with the parameter ϕ set to zero.

The analytical solution for the macroscopic velocity profile (Eq. (36)) is validated in Fig. 15 for the case of a combined Couette-Poiseuille flow subjected to either favorable ($\mathcal{R} = -2$) or adverse ($\mathcal{R} = +2$) pressure gradient, with the channel bounded from the bottom by a permeable layer constructed of streamwise-elongated cylindrical inclusions ($\theta = 0.5$). To assess sensitivity of the model accuracy to the value of $\epsilon = \ell/H$, departing from the case of perfect separation of length scales (at $\epsilon \to 0$), four configurations of the porous bed are

considered with ϵ increased from 0.4 to 6. Interestingly, both the first and the second-order solutions are able to predict the flow separation at the permeable boundary for $\mathcal{R} = +2$, yet it is clear that upgrading the effective boundary conditions to second order (by including effects of the interface permeability) significantly improves accuracy of the model predictions at the larger values of ϵ; this is consistent with the previous discussion in Section 3.1.3 for the corresponding case of Poiseuille flow.

We now elaborate a bit further on the predictions of the first-order accurate analytical solution, which has been proven to describe fairly well the macroscopic velocity profile at relatively low values of ϵ. The Couette-Poiseuille flow is now assumed to be controlled only by the parameters $\mathcal{R}$ and $\Lambda = \epsilon\lambda$. In Fig. 16, analytical predictions for the profile $\mathcal{U} = \mathcal{U}(Y)$, corresponding to different values of $\mathcal{R}$, are plotted for four values of the slip coefficient Λ, gradually deviating from the case of a smooth, impermeable boundary ($\Lambda = 0$). It is clear
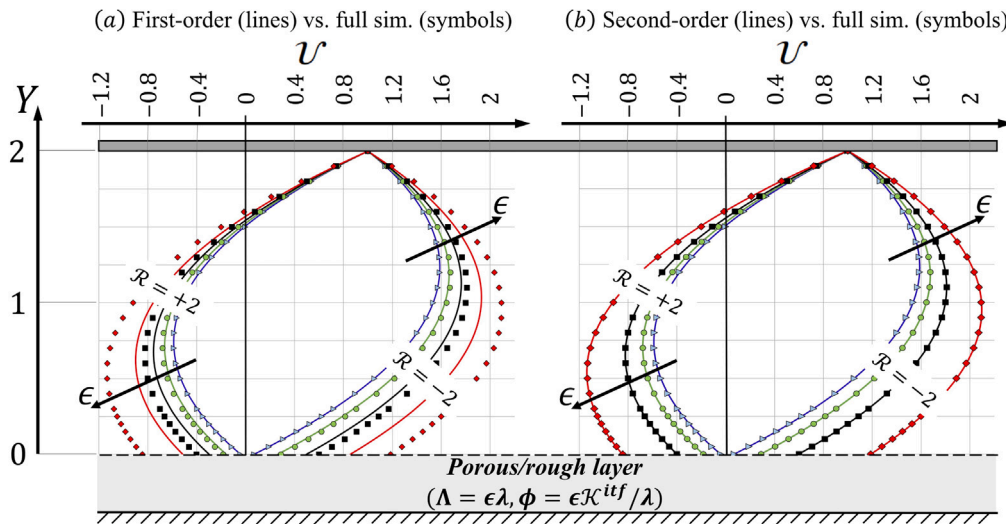
Fig. 15. *Generalized Couette-Poiseuille flow ($\mathcal{R} = \pm 2$) in a channel bounded from the bottom by a porous substrate consisting of an inline pattern of longitudinal cylinders with porosity $\theta = 0.5$ ($\lambda = 0.0688$, $\mathcal{K}^{itf} = 0.0056$). Four values of ϵ are tested, i.e. $\epsilon = 0.4$, 1.6, 3.2, and 6. Results of the full simulations (symbols) are used to validate the analytical solution for $\mathcal{U}$ (lines), based on either the first-order (a) or the second-order (b) model.*

that the slip velocity at the permeable/rough boundary and the bulk, channel-averaged velocity increase with Λ for the case of no pressure-gradient or favorable pressure gradient (Figs. 16(a) and (b)); the same effect of Λ, progressively less pronounced, is observed in the case of adverse pressure gradient, provided that the value of $\mathcal{R}$ is sufficiently small for backflow not to appear. At $\mathcal{R} = \mathcal{R}_{cr} = 0.5$, all profiles coincide regardless of the value of Λ, with vanishing slip velocity and velocity gradient at the bottom boundary; this is the critical threshold for separation (Fig. 16(d)). Larger values of $\mathcal{R}$ lead to progressively larger portion of the channel interested by backflow, and the larger the parameter Λ is, the more amplified the backflow becomes (cf. Fig. 16(e)). A summary of the first-order results obtained, in terms of $\mathcal{U}'_{slip}$ and $\mathcal{U}_{ch}$, are shown in Fig. 16(f) and (g), for the values of Λ considered.

The conclusions to be inferred from Fig. 16 would be modified to some extent in case the parameters of the problem were such that upscaling were needed up to order two in ϵ, or consideration of near-wall nonlinear effects were necessary. This is, however, a trivial task to pursue, since Eqs. (36) and (37) remain valid, and one has simply to employ the appropriate values of Λ and ϕ, possibly via an Oseen-based approximation. For example, if second-order accurate effective boundary condition had been used, it is trivial to find that the critical limit of the dimensionless pressure gradient would be anticipated, i.e. $\mathcal{R}_{cr} = 0.5/(1 + \phi)$; thus, for instance, if $\phi \approx 0.5$ (as for the pattern considered in Fig. 15 with $\epsilon = 6$), it would be $\mathcal{R}_{cr} \approx 0.34$.

4. Conclusions

The laminar flow in a channel is crucially sensitive to the small-scale features of the rough/porous bounding walls; this is assessed here for the steady, incompressible, fully developed flow driven by a constant pressure gradient and/or by motion of a wall at a prescribed constant speed (i.e., pure Poiseuille, pure Couette, and combined Couette-Poiseuille flows). The microscopic pattern of the rough/permeable wall is assumed not to have a preferential orientation at an angle different from 0 or 90 degrees from the direction of the pressure gradient since, should that be the case, a near-wall transverse velocity component would appear [21]. In other words, the wall/substrate must be such that the Navier slip tensor has components only along the principal axes of the flow. These are quite general hypothesis, satisfied by many natural/engineered wall textures [12]. Analytical solutions of the

Navier–Stokes equation governing the one-directional flows, $\hat{u} = \hat{u}(\hat{y})$, exist, subject to BJS-like conditions which apply at a *virtual planar interface* in $\hat{y} = 0$ and/or $\hat{y} = 2H$, next to the physical boundaries. The classical upscaling approach is tenable as long as the parameter ϵ, ratio of the microscopic length scale to half the channel height, remains sufficiently small and the flow regime in close vicinity of the walls is Stokes-like. As a rule of thumb, the approach is found to be reliable until $\epsilon Re_{\tau} \approx 10$. Under these conditions, the *generalized Poiseuille* solution is very accurate when compared against feature-resolving simulations of the flow in channels with different combinations of wall textures. The *generalized combined Couette-Poiseuille* solution was tested under favorable/adverse pressure gradients, and its accuracy in predicting possible backflow next to the fluid-porous interface was highlighted.

One of the most important issues addressed in this article is how to efficiently incorporate the effects of near-wall advection into the homogenization procedure when ϵRe_{τ} is larger than about 10. For this purpose, an *Oseen's approximation* was employed to linearize the convective acceleration terms in the momentum conservation equations governing the microscale problem. Numerical solutions of the closure problems revealed a decreasing trend of the model coefficients, for any given tested microstructure, as inertial effects became significant. It was confirmed, via extensive validation, that the adjusted approach can widen the applicability range of the homogenized solution considerably. Nonetheless, should flow instabilities be present in the domain (e.g., at relatively high Reynolds numbers) in the form of vortex shedding next to the protrusions/grains or, eventually, transition to turbulence, homogenization would become a more complex undertaking. For instance, tackling near-wall advection with Oseen's linearization in the presence of such instabilities may be questionable, and a fully nonlinear model is probably needed; this could be achieved by the use of adjoint homogenization [12]. In addition, when near-wall transient effects are significant, they should be considered in the upscaling framework, and sufficiently large *representative elementary cells* of the microscopic domain (possibly larger than a single geometric unit cell) must be identified [24]. Further, under turbulent flow conditions it is necessary to define a three-directional effective velocity at the fictitious wall, even if the mean flow is one-directional. This is important since turbulent fluctuations along directions both tangent and normal to the fictitious interface considerably affect the behavior of the turbulent boundary layer and, therefore, the skin-friction drag [12, 14,20,27–29].
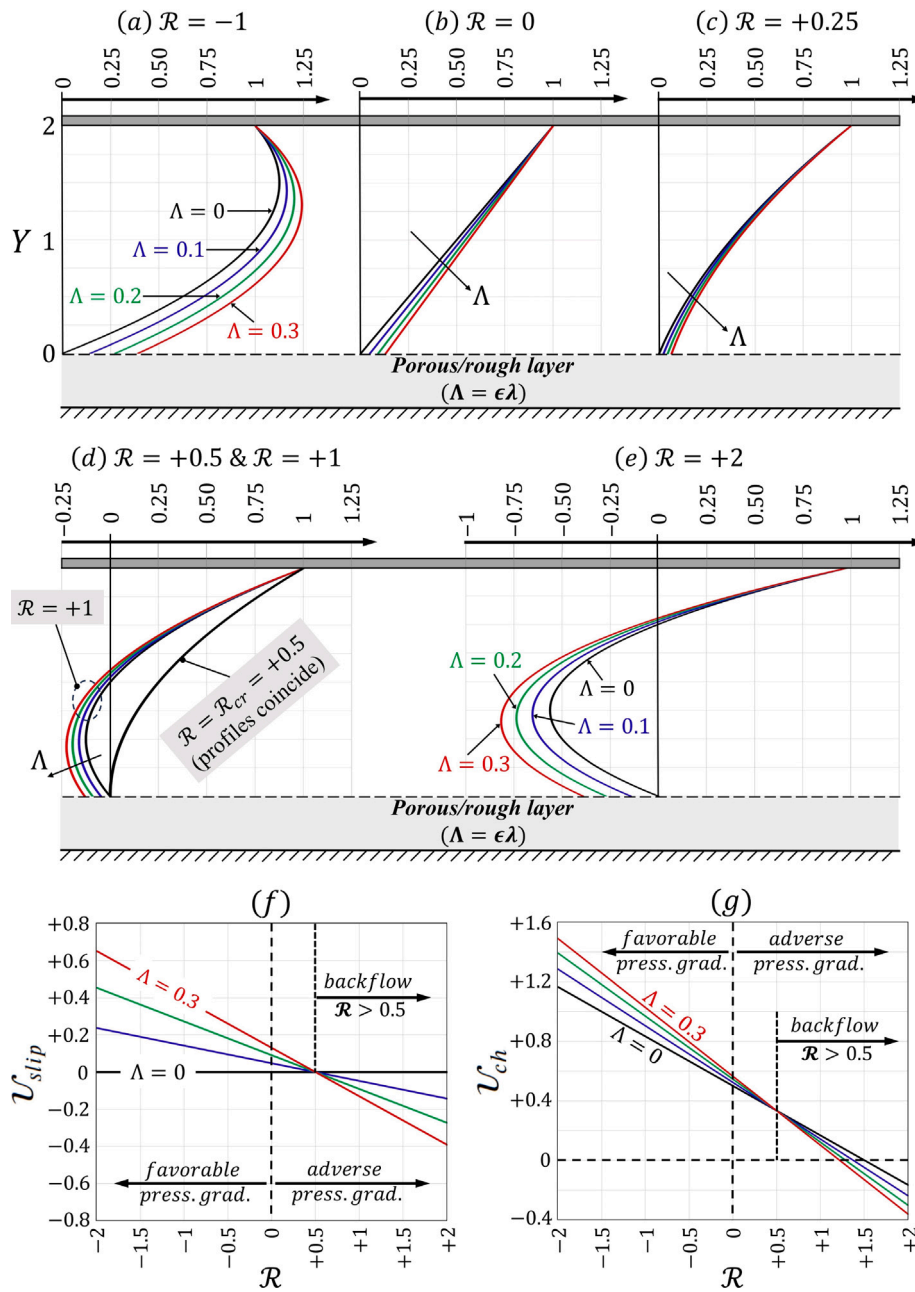
Fig. 16. Predictions of the first-order analytical solution ($\phi = 0$) for the behavior of the *generalized Couette-Poiseuille* flow, with the parameter $\Lambda = \epsilon\lambda$ characterizing the bottom boundary of the channel varied between 0 (smooth, impermeable) and 0.3. The macroscopic velocity profiles are plotted in panels (a–e) for different values of $\mathcal{R}$, and the trends of the slip and the channel-averaged velocities are displayed in frames (f) and (g).

The analysis conducted attests to the effectiveness of multiscale homogenization and provides a low-cost framework for understanding the large-scale features of laminar flows over rough/permeable surfaces. One advantage of the approach is that the effective boundary conditions adopted are free of empirical parameters; the macroscopic coefficients involved are available from well-defined closure problems to be solved in a microscopic elementary cell, and can be evaluated systematically for walls characterized by different types of non-uniformity, including the effects of porosity, roughness, superhydrophobicity, compliance, etc. Several results for λ and $\mathcal{K}^{itf}$ have been recently computed (e.g. Refs. [14–20]) and can be used to assess the effect of a variety of rough/porous micro-structured media. These results (and others that might easily be obtained for different microscopic geometries) may serve for the inverse design of wall patterns, to satisfy specific constraints, or for the validation of newly developed computational fluid dynamics codes.

Declaration of competing interest

The authors declare that they have no known competing financial interests or personal relationships that could have appeared to influence the work reported in this paper.

Data availability

Data will be made available on request.

References

[1] G.S. Beavers, D.D. Joseph, Boundary conditions at a naturally permeable wall, J. Fluid Mech. 30 (1) (1967) 197–207, http://dx.doi.org/10.1017/S0022112067001375.

[2] R.E. Larson, J.J.L. Higdon, Microscopic flow near the surface of two-dimensional porous media. Part 1. Axial flow, J. Fluid Mech. 166 (1986) 449–472, http://dx.doi.org/10.1017/S0022112086000228.

[3] M. Sahraoui, M. Kaviany, Slip and no-slip velocity boundary conditions at interface of porous, plain media, Int. J. Heat Mass Transfer 35 (4) (1992) 927–943, http://dx.doi.org/10.1016/0017-9310(92)90258-T.

[4] D.A. Nield, The Beavers–Joseph boundary condition and related matters: A historical and critical note, Transp. Porous Media 78 (3) (2009) 537–540, http://dx.doi.org/10.1007/s11242-009-9344-y.

[5] P.G. Saffman, On the boundary condition at the surface of a porous medium, Stud. Appl. Math. 50 (2) (1971) 93–101, http://dx.doi.org/10.1002/sapm197150293.

[6] G. Neale, W. Nader, Practical significance of Brinkman's extension of Darcy's law: Coupled parallel flows within a channel and a bounding porous medium, Can. J. Chem. Eng. 52 (4) (1974) 475–478, http://dx.doi.org/10.1002/cjce.5450520407.

[7] K. Vafai, S.J. Kim, Fluid mechanics of the interface region between a porous medium and a fluid layer—An exact solution, Int. J. Heat Fluid Flow 11 (3) (1990) 254–256, http://dx.doi.org/10.1016/0142-727X(90)90045-D.

[8] J.-L. Auriault, About the Beavers and Joseph boundary condition, Transp. Porous Media 83 (2) (2010) 257–266, http://dx.doi.org/10.1007/s11242-009-9435-9.

[9] E. Eggenweiler, I. Rybak, Unsuitability of the Beavers–Joseph interface condition for filtration problems, J. Fluid Mech. 892 (2020) A10, http://dx.doi.org/10.1017/jfm.2020.194.

[10] E. Eggenweiler, I. Rybak, Effective coupling conditions for arbitrary flows in Stokes–Darcy systems, Multiscale Model. Simul. 19 (2) (2021) 731–757, http://dx.doi.org/10.1137/20M1346638.

[11] P. Strohbeck, E. Eggenweiler, I. Rybak, A modification of the Beavers-Joseph condition for arbitrary flows to the fluid-porous interface, Transp. Porous Media 147 (3) (2023) 605–628, http://dx.doi.org/10.1007/s11242-023-01919-3.

[12] A. Bottaro, Flow over natural or engineered surfaces: An adjoint homogenization perspective, J. Fluid Mech. 877 (2019) P1, http://dx.doi.org/10.1017/jfm.2019.607.

[13] U. Lācis, S. Bagheri, A framework for computing effective boundary conditions at the interface between free fluid and a porous medium, J. Fluid Mech. 812 (2017) 866–889, http://dx.doi.org/10.1017/jfm.2016.838.

[14] U. Lācis, Y. Sudhakar, S. Pasche, S. Bagheri, Transfer of mass and momentum at rough and porous surfaces, J. Fluid Mech. 884 (2020) A21, http://dx.doi.org/10.1017/jfm.2019.897.

[15] Y. Sudhakar, U. Lācis, S. Pasche, S. Bagheri, Higher-order homogenized boundary conditions for flows over rough and porous surfaces, Transp. Porous Media 136 (1) (2021) 1–42, http://dx.doi.org/10.1007/s11242-020-01495-w.

[16] S.B. Naqvi, A. Bottaro, Interfacial conditions between a free-fluid region and a porous medium, Int. J. Multiph. Flow 141 (2021) 103585, http://dx.doi.org/10.1016/j.ijmultiphaseflow.2021.103585.

[17] A. Bottaro, S.B. Naqvi, Effective boundary conditions at a rough wall: A high-order homogenization approach, Meccanica 55 (9) (2020) 1781–1800, http://dx.doi.org/10.1007/s11012-020-01205-2.

[18] E.N. Ahmed, A. Bottaro, G. Tanda, A homogenization approach for buoyancy-induced flows over micro-textured vertical surfaces, J. Fluid Mech. 941 (2022) A53, http://dx.doi.org/10.1017/jfm.2022.320.

[19] E.N. Ahmed, Natural-convection heat transfer from regularly ribbed vertical surfaces: Homogenization-based simulations towards a correlation for the Nusselt number, Numer. Heat Transf. A Appl. 83 (9) (2023) 991–1013, http://dx.doi.org/10.1080/10407782.2023.2165993.

[20] E.N. Ahmed, S.B. Naqvi, L. Buda, A. Bottaro, A homogenization approach for turbulent channel flows over porous substrates: Formulation and implementation of effective boundary conditions, Fluids 7 (5) (2022) 178, http://dx.doi.org/10.3390/fluids7050178.

[21] H.A. Stone, A.D. Stroock, A. Ajdari, Engineering flows in small devices: Microfluidics towards a lab-on-a-chip, Annu. Rev. Fluid Mech. 36 (2004) 381–411, http://dx.doi.org/10.1146/annurev.fluid.36.050802.122124.

[22] P.J. Schmid, D.S. Henningson, Stability and Transition in Shear Flows, Springer NY, New York, 2001.

[23] M. Sano, K. Tamai, A universal transition to turbulence in channel flow, Nat. Phys. 12 (3) (2016) 249–253, http://dx.doi.org/10.1038/nphys3659.

[24] M. Agnaou, D. Lasseux, A. Ahmadi, From steady to unsteady laminar flow in model porous structures: An investigation of the first Hopf bifurcation, Comput. & Fluids 136 (2016) 67–82, http://dx.doi.org/10.1016/j.compfluid.2016.05.030.

[25] E.N. Ahmed, A. Bottaro, Flow through porous metamaterials formed by TPMS-based unit cells: Effects of advection, Eur. J. Mech. B Fluids 100 (2023) 202–207, http://dx.doi.org/10.1016/j.euromechflu.2023.04.002.

[26] L. Buda, Drag Reduction Over Rough Permeable Surfaces: a Homogenized-Based Approach (Master's Thesis in Physics), University of Genoa, Italy, 2021, Available at http://www.dicat.unige.it/bottaro/Presentation%20group/Thesis_Buda.pdf.

[27] P. Orlandi, S. Leonardi, DNS of turbulent channel flows with two- and three-dimensional roughness, J. Turbul. 7 (2006) N73, http://dx.doi.org/10.1080/14685240600827526.

[28] P. Orlandi, S. Leonardi, R.A. Antonia, Turbulent channel flow with either transverse or longitudinal roughness elements on one wall, J. Fluid Mech. 561 (2006) 279–305, http://dx.doi.org/10.1017/S0022112006000723.

[29] P. Orlandi, S. Leonardi, Direct numerical simulation of three-dimensional turbulent rough channels: Parameterization and flow physics, J. Fluid Mech. 606 (2008) 399–415, http://dx.doi.org/10.1017/S0022112008001985.